A 3D multi-material cell-centered indirect Arbitrary Lagrangian-Eulerian scheme using compressive limiters

S. Guisset[1,2], S. Peluchon[1], A. Colaitis[3], J. Breil[1]

Abstract

In recent decades, diffuse interface methods have become popular for the simulation of multi-material flows. They consider regions where the materials may be artificially mixed and interfaces are then considered as diffuse zones. In this document, a cell-centered indirect arbitrary Lagrangian-Eulerian diffuse interface strategy is presented for solving 3D multi-material equations. The use of a compressive limiter enables to prevent excessive numerical diffusion during the remapping step. It also allows the same treatment for pure and mixed cells, the same framework for dispersed or separated phases, robust multi-material simulations and easy multiphysics extensions. To address the discrete total energy conservation issue, the total kinetic energy is remapped to correct the material internal energies. It is proved that the correction terms are positive thus enforcing thermodynamics consistency. Last but not least, stiff multi-material test cases, involving fluids with highly contrasted equations of states are carried out, demonstrating the robustness of the overall numerical strategy.

Key words: Multi-material flows simulation, diffuse interfaces, Arbitrary Lagrangian-Eulerian hydrodynamics, compressive limiters, multi-dimensional.

[1]CEA/CESTA, 15 Avenue des Sablières CS 60001, 33116 Le Barp cedex, France
[2]Corresponding author: sebastien.guisset@cea.fr
[3]Laboratory for Laser Energetics, 250 East River Rd, Rochester, NY 14623-1212

1 Introduction

Multi-material flows are complex and ubiquitous phenomena in nature and industry. In many applications, material interfaces are treated as discontinuities since their widths are substantially smaller than the macroscopic length scales. Over the past decades, the numerical simulation of these interfaces has been extensively studied by the community and various models and numerical approaches have been proposed. Two distinct strategies have emerged. The first category, referred to as sharp interface methods, deals with clearly separated materials and the interface corresponds to the boundary between them. Here no mixing between materials is allowed. The second category, referred to as diffuse interface methods, considers areas in which the materials may artificially mix with each other. Interfaces are then seen as diffused zones. This last strategy, has become popular over the past few decades. Several factors can be cited to explain this popularity. Firstly, since the material interfaces are allowed to spread over a certain width, geometrical technicalities are alleviated. This leeway enables to bypass the unpleasant 3D geometrical interfaces reconstruction step. Secondly, additional physical modeling such as surface tension, drag force, capillarity among others [19] can be incorporated more naturally. Thirdly, the development of efficient anti-diffusive methods [6, 47, 48] combined with an increased computational power, largely contributed in reducing the natural numerical smearing of the material interfaces. We refer to [49, 39, 3, 42, 33] and the references therein for more details on diffuse interface strategies.

Regarding the modeling aspects, several approaches cohabit within the diffuse interface framework. The variations are mainly due to the degree of refinement selected. In general, it follows the number of equations used to model the multi-material flow. For example, four-equation models simply consider a transport equation to model the interface advection in addition to mixture equations (i.e., equations on the average density, momentum and energy of the mixture). It should be emphasized that material densities and internal energies are not available in this case. Alternatively, a much more accurate description of the mixture is reached by working with seven-equations models [9]. In this instance all material variables are accessible (density, momentum, internal energy and volume fraction of each material). Unfortunately, the numerical discretisation of such models can be challenging. For example, the thermodynamics aspects (material entropy dissipation) at the discrete level are often omitted, while being crucial in some applications.

Five-equation models constitute a balance between the two aforementioned models, providing a physical sound modeling without losing too much simplicity. In this framework, all material thermodynamic states are available (sometimes implicitly) but only the mixture velocity is defined. Inside the five-equation model category, various models exist [4, 43]. They all coincide on the mixture momentum and energy as well as material mass equations while differences are observed on the material internal energies, densities, volume fractions, pressures or entropies.

The starting point of this paper is a five-equation model which may be obtained thanks to a conditional averaging procedure [30, 37, 20]. This model is isentropic for each material since all the fluctuation terms obtained from the averaging procedure are dropped. This model may then be seen as a backbone model on which additional physical terms may be added depending on the applications investigated. In the present document we focus on the equal strain closure which assumes that the material volumic fractions stay constant during the Lagrangian phase. In this case, all materials are compressed or expanded with the same rate. This assumption is attractive since it is numerically simple and is relevant enough for various multiphase applications [12]. Some limitations should be pointed out since when working with contrasted equations of state (e.g. air and water) a strong non-physical pressure decoupling may appear in mixed cells. This decoupling may be problematic in some applications resulting in a crash of the code. For these reasons the equal pressure assumption is sometimes privileged, we refer to [7] in which this point has been investigated in details.

On the numerical side, the numerical strategy presented in this document lies in the class of arbitrary Lagrangian-Eulerian (ALE) method [11, 28, 31]. Usually, ALE algorithms are organised in two groups. The first one, referred in the literature as "direct ALE" considers the resolution of the flows equations moving on an arbitrary mesh. With this approach the transport terms are directly taken into account. The second one, known as "Lagrangian plus Remapping" or indirect ALE methods is the one we consider in the present document. With this approach, an explicit Lagrangian phase is solved in which the mesh follows the fluid velocity. This Lagrangian formalism is particularly adapted for multi-material flows since interfaces are captured exactly. However, if the flow encounters large deformations, the mesh quality is in general strongly affected with possible mesh entanglement. In this framework, a mesh regularisation procedure is needed with the desire to modify the node positions to improve the overall mesh quality. Of course, the nu-

merical solutions should be remapped on this regular mesh. This last stage is critical especially when working with multi-material flows and must be carefully addressed [40]. This overall "Lagrangian plus Remapping" strategy is particularly efficient since the remapping phase on a regular mesh ensures the robustness of the method while keeping some attractive feature of the Lagrangian step. In addition, this formalism greatly eases the control of the material entropy dissipation since the thermodynamics aspects are separated from the transport part.

Over the last decades, various numerical methods have been designed to solve the Lagrangian hydrodynamic equations. We do not intend to review them all in this introduction. We restrict ourself to mention the most popular ones. Among them are the "staggered schemes" in which the kinematic variables (nodes velocity and nodes position) are computed at the nodes while the thermodynamics quantities are evaluated at the center of the cells. Starting from the pioneer works [54, 55] various extensions have been made over the years [14, 36] and are used today in diverse engineer applications. A second popular class of numerical methods is the "cell-centered finite volume schemes". The schemes are based on the pioneer work of Godunov [26] and consider cell-centered quantities. In this case, the nodes velocities are obtained from a nodal solver. Over the years, various multi-directional extensions have been proposed [22, 38] with various accuracy enhancement methods [13, 15, 29]. It should also be mentioned that finite element methods are largely investigated for solving Lagrangian hydrodynamics equations [23, 50].

Along the indirect ALE methodology, the regularization step is a delicate one. While the objective is to increase the overall mesh quality, one also would like to maintain some interesting Lagrangian features. In the present work, the mesh regularisation procedure presented in detail in [27] is directly used. The regularisation step is not the original part, so we will not review all the regularisation algorithm found in the literature. For the interested reader, we simply refer to some of the most popular ones [56, 57, 35, 34].

The 3D multi-material remapping step is explained carefully in this document in which a 3D sweeping technique is used extensively. Introduced in [41], this strategy is popular since the expensive intersections between two 3D meshes are not required. Seen as a compatibility exercice, this method boils down to compute the volume integral of a new cell starting from the integral of the old cell plus the contributions of the swept regions by the displacement of the cell faces. This sweeping approach is favored over the

cell-intersection based method which can be expensive in this 3D setting [53].

The present work may be seen as a general extension of two previous studies [27, 7]. More exactly, the numerical study presented starts from [27] in which it has been shown that the ideas presented in [32, 59], may be used inside a 3D hydrodynamics code, to perform reliable regularization steps. In addition, the remapping step uses extensively the geometrical splitting procedure of the Lagrangian phase thus ensuring the compactness of the overall algorithm. The multi-material aspects were not addressed at all. On the contrary in [7], some multi-material aspects have been investigated. To be more specific, a cell-centered Lagrangian scheme has been presented for a multi-material model with equal pressure assumption. Nonetheless, only first order numerical strategies were investigated for the Lagrangian and remapping steps. Moreover, the study was restricted to 1D-2D geometries, mesh regularisation aspects were not addressed and no numerical treatment was proposed to deal with the natural smearing of the material interfaces.

In our opinion, the originality of this work stems from multiple factors. Firstly, the present document considers material interfaces as diffuse areas in which materials may artificially mix with each other. As aforementioned, this diffuse interface strategy recently gained popularity since the inherent numerical smearing of the interfaces can be largely mitigated by anti-diffusive techniques [49, 39, 47, 48]. On this point, the use of a compressive limiter is presented to prevent an excessive numerical diffusion during the material volume fractions remapping. This strategy is developed because of its simplicity. This can be contrasted with the complexity of intersection-based 3D multi-material remapping, such as presented in [1], which combines 3D interface reconstructions, a surrogate volume approach to ensure conservation properties and flux-corrected remapping to ensure convexity of the remapping. Furthermore, it allows the same treatment for pure and mixed cells, the same framework for dispersed or separated phases, robust multi-material simulations and easy multiphysics extensions. It should be stated that, even if the compressive limiters largely mitigate the diffusion of the material interfaces, for coarse meshes the numerical results obtained are still diffused. In addition, it should be mentioned that for any mesh refinement (coarse or refined), geometry interface reconstruction based strategies are more accurate than diffused interface methods. Therefore, in this document, it is investigated if the diffuse interface approach can be used as an interesting compromise between accuracy (by limiting the numerical smearing) and simplicity (compared to interfaces reconstruction strategies).

Secondly, the remapping procedure presented consists in remapping the material internal energies. This point is sensitive since a naive remapping does not enforce the discrete total energy conservation. To tackle this issue, the total kinetic energy is also remapped to correct the material internal energies. To be more specific, the correction strategy presented in [21, 2] is used in this cell-centered framework, it enables the discrete energy conservation and it is proved that the material internal energies corrections are positive thus enforcing a correct thermodynamics consistency. We also mention that an internal energy formulation has been chosen for the multi-material Lagrangian step. At first order, this approach is equivalent to the strategy proposed in [12], this point is discussed in this paper.

Finally, stiff multi-material test cases are investigated. Some of the multi-material studies found in the literature restrict themselves to materials described by perfect gas equation of state for which only the polytropic index of gas varies. In this case, there is no stiffness due to material compressibility difference. Numerical tests involving fluids with contrasted equations of state (e.g. air and water) are presented. This demonstrates the robustness of the overall numerical strategy.

The present work should be put into perspective with several existing works found in the literature on 3D multi-material ALE aspects. We mention the code ALEGRA [46] developed at Sandia National Laboratories. In the framework of cell-centered Lagrangian scheme, we mention [18], in which a 3D cell-centered numerical scheme is used in combination with a Flux-Corrected-Transport (FCT) remap for the simulation of multiphase flows. In this work an interface-aware subscale closure model and a multi-material remap strategy are used. We also mention [5] where the simulation of 3D multi-material ALE hydrodynamics is studied based on high-order finite elements. More recently, in [53] conservative interpolation of multi-material fields, free of mesh-mesh intersections, have been proposed and used to perform effective remapping step in a multi-material Arbitrary Lagrangian-Eulerian code.

The document is organized as follows. Firstly, the overall governing equations are presented and the multi-materials aspects are recalled. In a second section, the 3D multi-material Lagrangian step is discussed. The numerical discretisation of the internal energy formulation is detailed. In particular, the procedure to arbitrarily distribute the total entropy production between the materials is described. The differences with the numerical strategy presented in [12] are also highlighted. In a third part, the 3D multi-material remapping is provided. The 3D sweeping procedure combined with the use of a compres-

sive limiter technique is introduced. This strategy enables to considerably limit the numerical smearing of the material interfaces. Moreover, remapping the total kinetic energy enables to correct the material internal energies to enforce the discrete total energy conservation. This section is concluded by proving that this correction ensures the positiveness of the material internal energies. Finally, numerous 3D multi-material test cases are carried out to assess the behavior of the overall numerical method. This last section starts with two pure remapping tests to assess the behavior of the compressive limiters. Then fully 3D multi-material tests are presented. This section is concluded with stiff multi-materials tests involving fluids with contrasted equations of state (e.g. air and water). This demonstrates the robustness of the proposed strategy.

2 Governing equations

A mixture made of an arbitrary number of materials is considered. The volume fraction of material k is denoted by α^k and its density by ρ^k. Inside a given volume V where a mass m^k of material k occupies a volume V^k, these quantities are defined as follows

$$\alpha^k = \frac{V^k}{V}, \qquad \rho^k = \frac{m^k}{V^k}.$$

The total density of the mixture denoted ρ is defined as

$$\rho = \frac{m}{V} = \sum_k \alpha^k \rho^k.$$

Similarly, specific internal energy of material k is denoted e^k. Likewise, a specific internal energy for the mixture denoted e is defined as

$$me = \sum_k m^k e^k.$$

Each material k has its own pressure denoted p^k and entropy η^k. The quantities ρ^k, e^k and p^k are related to each other through an equation of state $p^k(\rho^k, e^k)$. Finally, the characteristic times at which material velocities relax to a common value are assumed to be significantly smaller than the characteristic times of observation. Therefore, only one common velocity $\boldsymbol{V}$ is

considered. Equations are written in terms of Lagrangian time derivatives which are defined by

$$\frac{d}{dt}\cdot = \frac{\partial}{\partial t}\cdot + \boldsymbol{V}\cdot\nabla\cdot .$$

The model is written for an arbitrary number of materials, each one of them being described by its own equation of state. The equations of state are arbitrary, provided they fulfill some standard thermodynamics constraints such as concavity of the entropy and having a real speed of sound. The present model writes

$$\begin{aligned}
\alpha^k\rho^k\frac{d}{dt}\left(\frac{1}{\alpha^k\rho^k}\right) &= \nabla\cdot\boldsymbol{V},\\
\rho\frac{d}{dt}\boldsymbol{V} &= -\nabla p,\\
\alpha^k\rho^k\frac{d}{dt}e^k &= -\alpha^k\rho^k p^k\frac{d}{dt}\left(\frac{1}{\rho^k}\right).
\end{aligned}$$

These equations are obtained thanks to a conditional averaging procedure introduced in [30] and summarized in [37] for non-miscible materials and in [20] for general mixtures. More precisely, starting from a single material Euler equations with discontinuous thermodynamic properties, these equations undergo a material-conditional averaging procedure which allows specific material quantities to be defined. All fluctuations appearing in the averaging procedure are then neglected and, as such, the model is naturally isentropic for each material. The internal energy equation of material k corresponds to Gibbs identity $de^k = -p^k d(1/\rho^k) + T^k d\eta^k$ with $d\eta^k = 0$ where η^k denotes the entropy associated to material k. In the following, the closure we consider is the so-called equal strain assumption [11] whereby all materials are assumed to experience the same volume deformation

$$\frac{1}{\rho}\frac{d}{dt}\rho = \frac{1}{\rho^k}\frac{d}{dt}\rho^k = \nabla\cdot\boldsymbol{V}.$$

As detailed in [24], combination of the previous equations yields

$$\frac{d}{dt}\left(\alpha^k\right) = 0.$$

This last equation is often introduced as a transport equation in Euler formalism

$$\frac{\partial}{\partial t}\left(\alpha^k\right) + \boldsymbol{V}\cdot\nabla\alpha^k = 0.$$

The density equation may be simplified and writes

$$\alpha^k \rho^k \frac{d}{dt}\left(\frac{1}{\rho^k}\right) = \alpha^k \nabla \cdot \boldsymbol{V},$$

while the internal energy evolution equation reads

$$\alpha^k \rho^k \frac{d}{dt} e^k = -\alpha^k p^k \nabla \cdot \boldsymbol{V},$$

and the total pressure $p = \sum_k \alpha^k p^k$. The closed model is hyperbolic with the speed of sound a of the mixture given as follows

$$a^2 = \sum_k \frac{m^k}{m} (a^k)^2.$$

This resulting model is widely used for the simulation of multi-material flows [12]. It should be point out that although if it is quite relevant for mixtures of similar materials, it may become unrealistic when dealing with contrasted equations of state. We refer to [7] where this point has been investigated and a cell-centered numerical scheme has been proposed for an equal pressure model. It should be noticed that with the updated Lagrangian formalism, the mesh moves with the fluid velocity. When considering practical applications this last point is critical and may often lead the mesh quality to be strongly reduced. In this case, the use of a regularization procedure becomes mandatory. Standard rezoning strategies use the positions of the nodes moved during the Lagrangian phase to build a new regularized grid. Finally, a remapping procedure is applied to remap all the conservative quantities onto the new grid.

3 3D multi-material Lagrangian scheme

3.1 Notations

In this section, the notations introduced in [25] are followed. The computational domain denoted $\omega(t)$ is paved with non-overlapping polyhedrons written ω_c such that $\omega(t) = \bigcup_c \omega_c$. A polyhedron is defined as a volume bounded by polygonal faces. It should be noticed that in this 3D context, the faces may not be planar. The definitions of outward normal and area are thus

not straightforward. In [25], the cells are subdivided by adding one point p_f^* for each face. This choice enables to prove the GCL property for the 3D Lagrangian phase (discrete compatibility relation between mass conservation and mesh geometry) and enforces a correct discrete symmetry preservation of the flow. The triangles created by the face splitting are denoted t_r. For completeness, we recall all the notations used

- $\mathcal{P}(c)$ is the set of nodes p of cell c without the nodes p_f^*,
- $\mathcal{F}(c,p)$ is the set of faces f of cell c and sharing point p,
- $\mathcal{C}(p)$ is the set of cells c sharing node p,
- $\mathcal{T}(c)$ is the set of all the triangles t_r resulting from the splitting of the faces of cell c,
- $\mathcal{T}(c,f)$ is the set of triangles t_r resulting from the splitting of the face f of cell c,
- $\mathcal{T}(c,f,p)$ is the set of triangles t_r resulting from the splitting of the face f of cell c and sharing point p.

Concerning the cell variables, the approach is that of a finite volume scheme. For physical quantities $\phi^k \in \left\{1/(\alpha^k\rho^k), 1/\rho^k, e^k\right\}$ related to a material k and a cell c, one thus defines the averaged quantities over the cell by

$$m_c^k = \int_{\omega_c} \alpha^k\rho^k dv, \qquad \phi_c^k = \frac{1}{m_c^k}\int_{\omega_c} \alpha^k\rho^k\phi dv,$$
$$m_c = \int_{\omega_c} \rho dv, \qquad \boldsymbol{V}_c = \frac{1}{m_c}\int_{\omega_c} \rho\boldsymbol{V} dv.$$

Defining these averaged quantities prepares for the use of Reynold's transport theorem which is used extensively the next section.

3.2 Numerical schemes

The multi-material Lagrangian scheme presented in this section extends the ideas presented in [27, 7] to the 3D multi-material settings. We point out that contrarily to [12] the internal energies are computed directly instead of solving a total energy equation. This approach enforces the discrete conservation of momentum and total energy while the semi-discrete entropy dissipation property is obtained for each material.

3.2.1 Total volume and momentum equations

Regarding the discretization of the mass and momentum equations, no significant changes are made from the usual Eucclhyd scheme [38]. The mass conservation equation, averaged over a Lagrangian cell, gives

$$m_c^k \frac{d}{dt}\left(\frac{1}{\alpha_c^k \rho_c^k}\right) = \int_{\partial\omega_c} \boldsymbol{V}\cdot\mathbf{n}ds = -\sum_{p\in\mathcal{P}(c)}\sum_{f\in\mathcal{F}(c,p)} s_{pf}\boldsymbol{V}_p\cdot\boldsymbol{n}_{pf}, \tag{1}$$

where the index c denotes that the quantity has been mass averaged over the considered cell. For the momentum conservation, Green's formula simply leads to

$$m_c\frac{d\boldsymbol{V}_c}{dt} = -\int_{\partial\omega_c} p\mathbf{n}d\mathbf{s} = -\sum_{p\in\mathcal{P}(c)}\sum_{f\in\mathcal{F}(c,p)} s_{pf}P_{cfp}\boldsymbol{n}_{pf}.$$

The nodal fluxes P_{cfp} and $\boldsymbol{V}_p$ are remaining unknowns to be determined. Following [25] in order to ensure a positive entropy production, the pressure jumps may be written in terms of the velocity jump as follow

$$P_{cfp} - p_c = Z_c\left(\boldsymbol{V}_c - \boldsymbol{V}_p\right)\cdot\boldsymbol{n}_{pf}, \tag{2}$$

where $Z_c = (\rho a)_c$ defines the acoustic impedance inside cell c, ρ the density of the mixture and a the mixture speed of sound. Considering the total momentum and energy conservation [38], the nodal velocity $\boldsymbol{V}_p$ may be computed by imposing a momentum balance around the node p. In this case, the node velocity $\boldsymbol{V}_p$ is defined by

$$\mathbb{M}_p\boldsymbol{V}_p = \boldsymbol{B}_p, \tag{3}$$

where

$$\mathbb{M}_p = \sum_{c\in\mathcal{C}(p)}\sum_{f\in\mathcal{F}(c,p)}\mathbb{M}_{cfp}, \qquad \mathbb{M}_{cfp} = s_{pf}Z_c\left(\boldsymbol{n}_{pf}\otimes\boldsymbol{n}_{pf}\right),$$
$$\boldsymbol{B}_p = \sum_{c\in\mathcal{C}(p)}\sum_{f\in\mathcal{F}(c,p)} s_{pf}\Big[p_c\boldsymbol{n}_{pf} + Z_c\left(\boldsymbol{n}_{pf}\otimes\boldsymbol{n}_{pf}\right)\boldsymbol{V}_c\Big].$$

Recall that the matrix $\mathbb{M}_p$ is positive definite thus invertible therefore the nodal velocity is easily computed. For completeness, we recall the definition of the face area vector $s_{pf}\boldsymbol{n}_{pf}$

$$s_{pf}\boldsymbol{n}_{pf} = \frac{1}{3}\left(\sum_{t_r\in\mathcal{T}(c,f,p)} s_{t_r}\boldsymbol{n}_{t_r} + \sum_{t_r\in\mathcal{T}(c,f)}\frac{1}{N_{p,f}}s_{t_r}\boldsymbol{n}_{t_r}\right), \tag{4}$$

and refer to [25] for its importance in enforcing the GCL condition. In this last equation, $N_{p,f}$ is the number of nodes on the face f, $\boldsymbol{n}_{t_r}$ the unit outward normal on the triangle t_r and the term $s_{pf}\boldsymbol{n}_{pf}$ is called face area vector and may be seen as the contribution of face f to the corner area vector [22] where the corner area vector writes $\boldsymbol{n}_p = \sum_{f\in\mathcal{F}(c,p)} s_{pf}\boldsymbol{n}_{pf}$.

3.2.2 Material internal energy equations

A naive discretization of the internal energy equation would consist in considering

$$m_c^k \frac{d}{dt} e_c^k = -\alpha_c^k p_c^k \sum_{p\in\mathcal{P}(c)} \sum_{f\in\mathcal{F}(c,p)} s_{pf}\mathbf{V}_p \cdot \boldsymbol{n}_{pf}.$$

However, when comparing this discretization with the standard single material scheme, one understands that some numerical dissipation needs to be added in order to stabilize the scheme. This numerical dissipation physically translates into entropy production so that the non-isentropic equations for each material k must be considered

$$m_c^k \frac{d}{dt} e_c^k = -\alpha_c^k p_c^k \sum_{p\in\mathcal{P}(c)} \sum_{f\in\mathcal{F}(c,p)} s_{pf}\mathbf{V}_p \cdot \boldsymbol{n}_{pf} + \int_{\omega_c} \alpha^k \rho^k T^k \frac{d}{dt}\eta^k dv.$$

In this equation, the discretization of the last term needs to be specified to enforce the chosen numerical viscosity for each material. The conservation equation of the total internal energy $\sum_k \alpha^k\rho^k e^k$ must be discretized according to the single material scheme (usual semi-discrete internal energy equation in the monomaterial case)

$$\begin{aligned}\sum_k m_c \frac{de_c^k}{dt} &= -\sum_{p\in\mathcal{P}(c)} \sum_{f\in\mathcal{F}(c,p)} s_{pf} P_{cfp}(\boldsymbol{V}_p - \boldsymbol{V}_c)\cdot\boldsymbol{n}_{pf}, \\ &= -p_c \sum_{p\in\mathcal{P}(c)} \sum_{f\in\mathcal{F}(c,p)} s_{pf}\boldsymbol{V}_p\cdot\boldsymbol{n}_{pf} + \sum_{p\in\mathcal{P}(c)} \sum_{f\in\mathcal{F}(c,p)} (\boldsymbol{V}_p - \boldsymbol{V}_c)\,\mathbb{M}_{cfp}\,(\boldsymbol{V}_p - \boldsymbol{V}_c)\,,\end{aligned}$$

which gives

$$\sum_k \int_{\omega_c} \alpha^k\rho^k T^k \frac{d}{dt}\eta^k dv = -\sum_{p\in\mathcal{P}(c)} \sum_{f\in\mathcal{F}(c,p)} (\boldsymbol{V}_c - \boldsymbol{V}_p)^T\,\mathbb{M}_{cfp}\,(\boldsymbol{V}_c - \boldsymbol{V}_p)\,.$$

The total entropy production now needs to be shared between materials through coefficients $\lambda_c^k > 0$ such that $\sum_k \lambda_c^k = 1$. The material discrete numerical viscosity is then written

$$\begin{aligned}\int_{\omega_c} \alpha^k \rho^k T^k \frac{d}{dt}\eta^k dv &= -\lambda_c^k \left[\sum_{p\in\mathcal{P}(c)} \sum_{f\in\mathcal{F}(c,p)} \left(\boldsymbol{V}_c - \boldsymbol{V}_p\right)^T \mathbb{M}_{cfp} \left(\boldsymbol{V}_c - \boldsymbol{V}_p\right) \right], \\ &= - \sum_{p\in\mathcal{P}(c)} \sum_{f\in\mathcal{F}(c,p)} \left(\boldsymbol{V}_c - \boldsymbol{V}_p\right)^T \mathbb{M}^k_{cfp} \left(\boldsymbol{V}_c - \boldsymbol{V}_p\right),\end{aligned}$$

with

$$\mathbb{M}^k_{cfp} = \lambda_c^k \mathbb{M}_{cfp}.$$

Concerning the choice of the coefficients λ^k we adapt the ideas presented in [16] to this context. For our test cases, we chose λ^k as the volume fraction of material k. Of course, other choices can be made to select the contribution of each material in the total entropy dissipation [8]. Finally, the space discretization of the material internal energy evolution equations writes

$$\begin{aligned} m_c^k \frac{de_c^k}{dt} &= -\alpha_c^k p_c^k \sum_{p\in\mathcal{P}(c)} \sum_{f\in\mathcal{F}(c,p)} s_{pf} \boldsymbol{V}_p \cdot \boldsymbol{n}_{pf} + \sum_{p\in\mathcal{P}(c)} \sum_{f\in\mathcal{F}(c,p)} \left(\boldsymbol{V}_p - \boldsymbol{V}_c\right) \mathbb{M}^k_{cfp} \left(\boldsymbol{V}_p - \boldsymbol{V}_c\right), \\ &= -\alpha_c^k \sum_{p\in\mathcal{P}(c)} \sum_{f\in\mathcal{F}(c,p)} s_{pf} P^k_{cfp} (\boldsymbol{V}_p - \boldsymbol{V}_c) \cdot \boldsymbol{n}_{pf}, \end{aligned} \tag{5}$$

where

$$P^k_{cfp} = p_c^k + Z_c \left(\boldsymbol{V}_c - \boldsymbol{V}_p\right) \cdot \boldsymbol{n}_{pf}.$$

In practice, second order extensions are used. The methodology considered to reach a second order space accuracy is exactly the one presented in [25]. We refer to this work and the references therein for a complete study on this subject. Concerning the time integration of the scheme, a direct predictor-corrector strategy is used. The resulting scheme is conservative with respect to momentum and total energy. In addition, similarly to [7], the semi-discrete entropy dissipation property holds true for each material. The proofs of these properties may be found in [7] and naturally extend in this 3D framework.

Remark. The difference with the strategy presented in [12] in now detailed. In [12], the procedure to compute the new material internal energies is as follows: first, the total energy evolution equation is solved. At this point,

the total internal energy equation can be deduced by removing the kinetic energy part (computed from the momentum equation). Secondly, the total entropy dissipation is computed and finally distributed according to the volume fraction of each material as follows

$$m^k \frac{d}{dt} e^k + p^k \frac{d}{dt} V^k = \alpha^k \left(m \frac{d}{dt} e + p \frac{d}{dt} V \right). \tag{6}$$

Solving a discrete version of this last equation is convenient since starting from a monomaterial code, only minor modifications are required. In addition, by using this last equation, the first order monomaterial scheme and the equal strain assumption gives

$$m_c^k \frac{d}{dt} e_c^k = -\alpha_c^k \sum_{p \in \mathcal{P}(c)} \sum_{f \in \mathcal{F}(c,p)} s_{pf} P_{cfp} (\boldsymbol{V}_p - \boldsymbol{V}_c) \cdot \boldsymbol{n}_{pf}, + \alpha_c^k (p_c - p_c^k) \frac{d}{dt} V_c, \tag{7}$$

where

$$P_{cfp} = p_c + Z_c \left(\boldsymbol{V}_c - \boldsymbol{V}_p \right) \cdot \boldsymbol{n}_{pf}.$$

Finally, by using (1), one can show that (7) and (5) are equivalent at first order. However, standard second order space extensions consider a linear reconstruction of a field ψ over a cell c and writes

$$\tilde{\psi}_c(\boldsymbol{x}) = \psi_c + \left(\nabla \psi \right)_c \cdot \left(\boldsymbol{x} - \boldsymbol{x}_c \right),$$

where $\tilde{\psi}_c(\boldsymbol{x})$ is the extrapolated value at point $\boldsymbol{x}$, $\left(\nabla \psi \right)_c$ is the gradient of ψ in the cell c and $\boldsymbol{x}_c$ the cell barycenter (or the cell centroid), we refer to [25] for more details. Pressure and velocity gradients are computed then the extrapolated stated are injected into the definitions of P_{cfp} and P_{cfp}^k. In this case, one understands that the two expressions do not coincide when summing over the materials since in the general case the material pressure gradients can be different from the total pressure gradient.

3.2.3 Time-discrete numerical scheme

The second order time discretisation follows the strategy presented in [25] in which a Predictor-Corrector method is used. Starting from a discrete solution which is completely known at time t^n, the fully discrete scheme writes as follows

• **Predictor step**

The intermediate velocity $\boldsymbol{V}_c^{(1)}$ and material internal energies $e_c^{k,(1)}$ are computed as

$$\boldsymbol{V}_c^{(1)} = \boldsymbol{V}_c^n - \frac{\Delta t}{m_c} \sum_{p\in\mathcal{P}(c)} \sum_{f\in\mathcal{F}(c,p)} s_{pf}^n P_{cfp}^n \boldsymbol{n}_{pf}^n,$$

$$e_c^{k,(1)} = e_c^{k,n} - \alpha_c^k \frac{\Delta t}{m_c} \sum_{p\in\mathcal{P}(c)} \sum_{f\in\mathcal{F}(c,p)} s_{pf}^n P_{cfp}^{k,n} \left(\boldsymbol{V}_p^n - \boldsymbol{V}_c^{(n+1/2)}\right) \cdot \boldsymbol{n}_{pf},$$

where

$$P_{cfp}^{k,n} = \tilde{p}_c^k(\boldsymbol{x}_p^n) + Z_c^n \left(\tilde{\boldsymbol{V}}_c(\boldsymbol{x}_p^n) - \boldsymbol{V}_p^n\right) \cdot \boldsymbol{n}_{pf}^n, \qquad P_{cfp}^n = \sum_k \alpha_c^k P_{cfp}^{k,n},$$

and the predictor intermediate velocity is defined by

$$\boldsymbol{V}_c^{(n+1/2)} = \frac{1}{2}\left(\boldsymbol{V}_c^n + \boldsymbol{V}_c^{(1)}\right).$$

• **Corrector step**

Starting from the known predicted solution, the new velocity $\boldsymbol{V}_c^{n+1}$ and material internal energies $e_c^{k,n+1}$ are computed from the initial and intermediate solutions

$$\boldsymbol{V}_c^{n+1} = \boldsymbol{V}_c^n - \frac{\Delta t}{2m_c} \sum_{p\in\mathcal{P}(c)} \sum_{f\in\mathcal{F}(c,p)} \left[s_{pf}^n P_{cfp}^n \boldsymbol{n}_{pf}^n + s_{pf}^{(1)} P_{cfp}^{(1)} \boldsymbol{n}_{pf}^{(1)}\right],$$

$$e_c^{k,(1)} = e_c^{k,n} - \alpha_c^k \frac{\Delta t}{2m_c} \sum_{p\in\mathcal{P}(c)} \sum_{f\in\mathcal{F}(c,p)} \Big[s_{pf}^n P_{cfp}^{k,n} (\boldsymbol{V}_p^n - \boldsymbol{V}_c^{n+1/2}) \cdot \boldsymbol{n}_{pf}^n + s_{pf}^{(1)} P_{cfp}^{k,(1)} (\boldsymbol{V}_p^{(1)} - \boldsymbol{V}_c^{n+1/2}) \cdot \boldsymbol{n}_{pf}^{(1)}\Big],$$

and the intermediate velocity (necessary for discrete energy conservation) is defined by

$$\boldsymbol{V}_c^{n+1/2} = \frac{1}{2}\left(\boldsymbol{V}_c^n + \boldsymbol{V}_c^{n+1}\right).$$

It should be mentioned that this time discretisation strategy doubles the computation time (compared to the standard forward Euler scheme). To address this issue the one-step Generalized-Riemann-Problem (GRP) integration procedure can be preferred [25].

4 ALE aspects and multi-material remapping

In this section a detailed presentation of the multi-material remapping step is provided. Since the regularisation procedure used in the next section follows exactly the one presented in [27], these aspects are put in Appendix. This multi-material remapping strategy relies extensively on the 3D sweeping procedure and a compressive limiter technique is introduced. These ideas, inspired by [52, 45, 60], enables to limit the numerical diffusion of the volume fraction. In addition, adapting the ideas presented in [21, 2] for staggered schemes, it is shown that the material internal energies may be corrected to enforce the discrete total energy conservation. Finally, it is proved that this correction enforces the positiveness of the material internal energies.

4.1 3D multi-material face sweeping strategy

The methodology presented in [41, 27] is now extended to the 3D multi-material context. A naive approach consists in following the strategy used in [27] including the multi-material variables. Consider ψ a given variable defined on a collection of non-overlapping polygons $\{c\}$, this variable is computed on a new collection of cells denoted $\{\tilde{c}\}$. More precisely, given the variable ψ on the collection $\{c\}$ we aim to compute

$$\psi_{\tilde{c}} = \frac{1}{V_{\tilde{c}}} \int_{\tilde{c}} \psi \, dv.$$

where $V_{\tilde{c}}$ is the volume of the new cell $\tilde{c}$. In this multi-material context the material masses, specific internal energies, volume as well as the total momentum must be remapped. Consequently, we choose ψ in the set

$$\psi \in \{\alpha^k \rho^k; \alpha^k; \alpha^k \rho^k e^k; \rho \boldsymbol{V}\}.$$

The volume $V_{\tilde{c}}$ of the new cell $\tilde{c}$ is obtained from the volume V_c of cell c plus the summation of the volumes (which are signed quantities) of the swept regions during the displacement of each triangle associated with a face (the triangles are obtained by the splitting of the cell faces). The swept region, starting from a cell c whose three constitutive points are denoted p, p^+, p^{++}, to the regularized one $\tilde{c}$, is denoted $\mathcal{P}_{\{p,\,p^+,\,p^{++}\}}$ (see Figure 1 in blue). The volume associated with this region is denoted $V(\mathcal{P}_{\{p,\,p^+,\,p^{++}\}})$. The new

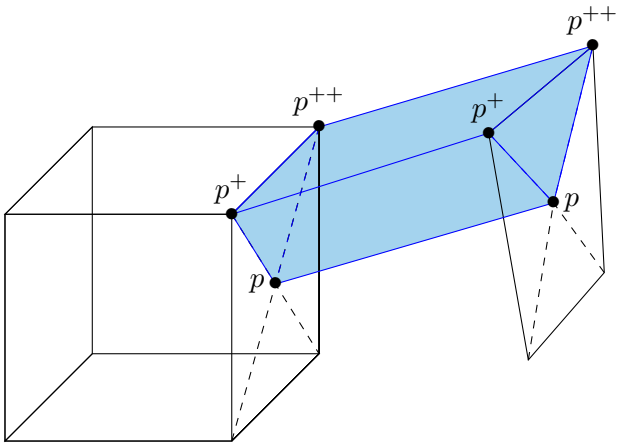

Figure 1: Representation of the swept region in blue, starting from an old triangle (formed by the points $\{p,\, p^{+},\, p^{++}\}$) to the new one.

volume $V_{\tilde{c}}$ can thus be expressed as follows

$$V_{\tilde{c}} = V_c + \sum_{\{p,\, p^{+},\, p^{++}\} \in \mathcal{T}(c)} V(\mathcal{P}_{\{p,\, p^{+},\, p^{++}\}}).$$

The computation of the new variable $\psi_{\tilde{c}}$ is then obtained by the following relation

$$\psi_{\tilde{c}} = \frac{1}{V_{\tilde{c}}} \left(\int_c \psi \, dv + \sum_{\{p,\, p^{+},\, p^{++}\} \in \mathcal{T}(c)} \int_{\mathcal{P}_{\{p,\, p^{+},\, p^{++}\}}} \psi \, dv \right), \tag{8}$$

where the last integral in the right-hand side in this last equation corresponds to the contribution to the flux of the swept region. Following [27] these integrals are computed using piecewise-linear reconstructions and a standard upwind strategy as follows

$$\int_{\mathcal{P}_{\{p,\, p^{+},\, p^{++}\}}} \psi \, dv = \begin{cases} \displaystyle\int_{\mathcal{P}_{\{p,\, p^{+},\, p^{++}\}}} \psi_{c^{+}}(\boldsymbol{x}) \, dv & \text{if} \quad V(\mathcal{P}_{\{p,\, p^{+},\, p^{++}\}}) > 0, \\ \displaystyle\int_{\mathcal{P}_{\{p,\, p^{+},\, p^{++}\}}} \psi_{c}(\boldsymbol{x}) \, dv & \text{if} \quad V(\mathcal{P}_{\{p,\, p^{+},\, p^{++}\}}) < 0, \end{cases}$$

where c and c^{+} represent the two neighboring Lagrangian cells that share the triangle $\{p,\, p^{+},\, p^{++}\}$ and $\psi_c(\boldsymbol{x})$ and $\psi_{c^{+}}(\boldsymbol{x})$ are their respective reconstructions of ψ. Piecewise-linear reconstructions of the variables on the Lagrangian

grid are considered. It is a standard procedure and has been extensively used in [24, 25]. The solution is sought under the form

$$\tilde{\psi}_c(\boldsymbol{x}) = \psi_c + (\boldsymbol{\nabla}\psi)_c \cdot (\boldsymbol{x} - \boldsymbol{x}_c)\,, \tag{9}$$

where ψ_c represents the known mean value in the cell and $(\boldsymbol{\nabla}\psi)_c$ a gradient of the quantity ψ in cell c. This gradient is computed using a least square procedure (we refer to [25] for the details). Finally, a standard Barth-Jespersen slope limiter approach is used to enforce the monotonicity of the reconstructed solution [10]. This point is developed in details in the next section.

4.2 Diffuse interfaces and compressive limiters

Contrarily to [24], in the present work we deal with interfaces as diffuse areas in which materials may artificially mix with each other. In the literature such methods are referred as diffuse interface methods. This category gained popularity since the inherent numerical smearing of the interfaces can be largely mitigated by anti-diffusive methods [6, 47, 48]. This last point is the focus of this section in which an anti-diffusive method based on compressive limiters is presented.

The linear reconstruction (9) may create non-physical extrema if the gradients are too steep. This result in numerical oscillations affecting the stability of the overall numerical scheme. In practice, to remove these unwanted oscillations the gradient terms are limited by considering a monotonicity criterion. Standard limiting strategy consists in applying a limiting scalar factor $\kappa_c \in [0, 1]$ to the gradient term so that the limited reconstructed value lies in range of the neighboring cell averaged valued. The limiting reconstructed value then writes

$$\psi_c^{lim}(\boldsymbol{x}) = \psi_c + \kappa_c\,(\boldsymbol{\nabla}\psi)_c \cdot (\boldsymbol{x} - \boldsymbol{x}_c)\,,$$

with

$$\psi_c^{min} \leq \psi_c^{lim}(\boldsymbol{x}) \leq \psi_c^{max}, \quad \boldsymbol{x} \in \omega_c, \tag{10}$$

where ψ_c^{min} and ψ_c^{max} corresponds to the minimum and maximum values of the scalar field ψ in the neighboring of cell c. In this work the face-based stencil is considered for the neighborhood of c. Since linear fields are

considered here, the extremum values are reached at the boundary of the cell i.e. at the cell nodes

$$\psi_c^{min} \leq \psi_c^{lim}(\boldsymbol{x}_p) \leq \psi_c^{max}, \quad \boldsymbol{x} \in \omega_c,$$

The limiting coefficient computation needs now to be defined. The monotonicity criterion (10) leads to the well-known Barth-Jespersen limiter [10]. In this case the limiter coefficient κ_c writes

$$\kappa_c = \min_{p \in \mathcal{P}(c)} \left(\kappa_{c,p} \right),$$

where

$$\kappa_{c,p} = \begin{cases} \min\left(\dfrac{\psi_c^{max} - \psi_c}{\tilde{\psi}_c(\boldsymbol{x}_p) - \psi_c}, 1 \right) & \text{if} \quad \tilde{\psi}_c(\boldsymbol{x}_p) > \psi_c, \\ \min\left(\dfrac{\psi_c^{max} - \psi_c}{\tilde{\psi}_c(\boldsymbol{x}_p) - \psi_c}, 1 \right) & \text{if} \quad \tilde{\psi}_c(\boldsymbol{x}_p) < \psi_c, \\ 1 & \text{if} \quad \tilde{\psi}_c(\boldsymbol{x}_p) = \psi_c, \end{cases} \tag{11}$$

This limiting strategy is applied for all the remapped quantities except for the material volume fraction. As a matter of fact, with this remapping procedure, the volume fraction will be diffused, resulting in a numerical smearing of the mixing zone between the different materials. In the spirit of [52], we propose to use a compressive limiter only for the material volume fraction remapping in order to obtain a more accurate representation of the discontinuities between the different materials considered. The idea consists in modifying the Barth-Jespersen limiter formula to sharpen the volume fraction field, which is initially piecewise constant. Standard Barth-Jespersen limiter requires the reconstruction to remain between the local minima and maxima of neighboring cells. To ensure that the reconstruction is exact for linear solutions on an admissible mesh, $\kappa_{c,p}$ must be equal to 1. In practise, in order to avoid spurious oscillations, $\kappa_{c,p}$ is taken smaller or equal to 1 by using formula (11).

At this point, to accurately reproduce a discontinuity, the standard limiter is modified to be compressive. To achieve this purpose, following the ideas presented in [52, 45], the preservation property of the linear field is dropped and the definition of $\kappa_{c,p}$ is modified by introducing a parameter $\beta \in [1, +\infty[$ to control the compressive feature of the limiter. The local

maximum principle is still enforced and the following definition is used

$$\kappa_{c,p} = \begin{cases} \min\left(\dfrac{\psi_c^{max} - \psi_c}{\tilde{\psi}_c(\boldsymbol{x}_p) - \psi_c}, \beta\right) & \text{if} \quad \tilde{\psi}_c(\boldsymbol{x}_p) > \psi_c, \\ \min\left(\dfrac{\psi_c^{max} - \psi_c}{\tilde{\psi}_c(\boldsymbol{x}_p) - \psi_c}, \beta\right) & \text{if} \quad \tilde{\psi}_c(\boldsymbol{x}_p) < \psi_c, \\ \beta & \text{if} \quad \tilde{\psi}_c(\boldsymbol{x}_p) = \psi_c. \end{cases}$$

In practice the compressive limiter is set to $\beta = 2$ on all material volume fractions while the classical limiter with $\beta = 1$ is used on the others remapped variables. The choice $\beta = 2$ allows to recover a compressive behavior similarly as the well-known 1D Superbee limiter [17, 45]. One should point out that this modification of the standard limiter strategy is particularly simple since almost no modification is required nor additional computational cost. In addition, the remapping strategy used for pure or mixed cells is identical. In the numerical test section, the impact of this compressive limiter is investigated. The theoretical computational cost remains unchanged whether the compressive limiter is applied or not, as no additional computations such as geometric operations are required. In practice, it is observed that the overall simulation time is unaffected, and there is no impact on the numerical time step for the test cases presented in the numerical tests section.

4.3 Enforcing total discrete energy conservation

The remapping procedure presented considers the remapping of total momentum and material internal energy are remapped so that, by denoting with a tilde symbol the remapped quantities we have

$$\sum_c \left(m\boldsymbol{V}\right)_c = \sum_{\tilde{c}} \left(m\boldsymbol{V}\right)_{\tilde{c}}, \qquad \sum_c \left(m^k e^k\right)_c = \sum_{\tilde{c}} \left(m^k e^k\right)_{\tilde{c}}.$$

However, it should be noticed that since the quantity $\boldsymbol{V}^2$ is not remapped, thus the total kinetic energy in the domain varies

$$\sum_{\tilde{c}} \frac{1}{2}\left(m\boldsymbol{V}^2\right)_{\tilde{c}} \neq \sum_{\tilde{c}} \frac{1}{2}\frac{(m\boldsymbol{V})^2_{\tilde{c}}}{m_{\tilde{c}}}.$$

More precisely, the total remapped kinetic energy in the domain is different from the total kinetic energy computed from the remapped mass and

momentum. This has serious consequence since the discrete total energy conservation is not enforced. This conservation issue may be addressed by adapting the procedure presented [21, 2] to this cell-centered approach. A first naive idea would consist in remapping the total energy and then correct the remapped internal energy accordingly. Unfortunately, this approach does not enforce the internal energy positiveness. A far better solution consists in remapping the kinetic energy $m\boldsymbol{V}^2/2$ and to evaluate the difference between the remapped kinetic energy and the one computed from the remapped mass and momentum. This quantity may then be used to modify the remapped material internal energy in each cell as follows

$$\left(m^k e^k\right)_{\tilde{c}}^{corrected} = \left(m^k e^k\right)_{\tilde{c}} + \frac{m_{\tilde{c}}^k}{m_{\tilde{c}}} \left(\frac{1}{2} \left(m\boldsymbol{V}^2\right)_{\tilde{c}} - \frac{1}{2} \frac{(m\boldsymbol{V})_{\tilde{c}}^2}{m_{\tilde{c}}} \right).$$

It is easy to show that these new definitions of material internal energies enable to enforce a total discrete energy conservation. In addition it is possible to demonstrate, in the simplified case of a first order remapping, that the correction term remains positive. To explain why this statement holds true, the idea presented in [27] can be applied to the correction term. For clarity, a simplified case is considered where only a triangle on a face has moved during the Lagrangian face. This idea may be extended in a more general case. For coherence with the previous notations, this triangle is denoted by its constitutive points p, p^+, p^{++}. In this simplified setting equation (8) rewrites

$$V_{\tilde{c}}\, \psi_{\tilde{c}} = V_c\, \psi_c + \int_{\mathcal{P}_{\{p,\, p^+,\, p^{++}\}}} \psi \, dv,$$

where

$$V_{\tilde{c}} = V_c + V(\mathcal{P}_{\{p,\, p^+,\, p^{++}\}}).$$

In the case of a first order remapping this last equation can be rewritten as follows

$$\left(V_c + V(\mathcal{P}_{\{p,\, p^+,\, p^{++}\}})\right)\, \psi_{\tilde{c}} = \left(V_c + V^-(\mathcal{P}_{\{p,\, p^+,\, p^{++}\}})\right)\, \psi_c + V^+(\mathcal{P}_{\{p,\, p^+,\, p^{++}\}})\psi_{c+},$$

where we have introduced the notation $V^{\pm} = \frac{1}{2}\left(V \pm |V|\right)$. A key point is to note that the first order remap simplifies to a straightforward linear interpolation between two states

$$\psi_{\tilde{c}} = \theta\, \psi_c + (1-\theta)\, \psi_{c^+}, \qquad \theta = \frac{V_c + V^-(\mathcal{P}_{\{p,\, p^+,\, p^{++}\}})}{V_c + V^+(\mathcal{P}_{\{p,\, p^+,\, p^{++}\}}) + V^-(\mathcal{P}_{\{p,\, p^+,\, p^{++}\}})}.$$

Consequently, since $\rho_{\tilde{c}} = m_{\tilde{c}}/V_{\tilde{c}}$ the computation of the new specific internal energy (computed from the remapped quantities) can be rearranged as follows

$$\left(e^k\right)_{\tilde{c}}^{corrected} = e_{\tilde{c}}^k + \frac{m_{\tilde{c}}^k}{m_{\tilde{c}}} \left(\frac{1}{2} \frac{(m\boldsymbol{V}^2)_{\tilde{c}}}{m_{\tilde{c}}^k} - \frac{1}{2} \frac{(m\boldsymbol{V})_{\tilde{c}}^2}{m_{\tilde{c}}^k m_{\tilde{c}}} \right) = e_{\tilde{c}}^k + \left(\frac{1}{2} \frac{(\rho\boldsymbol{V}^2)_{\tilde{c}}}{\rho_{\tilde{c}}} - \frac{1}{2} \frac{(\rho\boldsymbol{V})_{\tilde{c}}^2}{\rho_{\tilde{c}}^2} \right).$$

This last equation also rewrites

$$\begin{aligned}
\left(e^k\right)_{\tilde{c}}^{corrected} &= e_{\tilde{c}}^k + \frac{1}{2\rho_{\tilde{c}}} \left(\left(\rho\boldsymbol{V}^2\right)_{\tilde{c}} - \frac{(\rho\boldsymbol{V})_{\tilde{c}}^2}{\rho_{\tilde{c}}} \right) \\
&= e_{\tilde{c}}^k + \frac{1}{2\rho_{\tilde{c}}} \left(\theta \left(\rho\boldsymbol{V}^2\right)_c + (1-\theta) \left(\rho\boldsymbol{V}^2\right)_{c^+} - \frac{1}{\rho_{\tilde{c}}} \left(\theta \left(\rho\boldsymbol{V}\right)_c + (1-\theta) \left(\rho\boldsymbol{V}\right)_{c^+} \right)^2 \right) \\
&= e_{\tilde{c}}^k + \frac{1}{2\rho_{\tilde{c}}} \Bigg(\theta\rho_c \boldsymbol{V}_c^2 + (1-\theta)\rho_{c^+} \boldsymbol{V}_{c^+}^2 \\
&\qquad - \frac{1}{\rho_{\tilde{c}}} \left(\theta^2 (\rho\boldsymbol{V})_c^2 + 2\theta(1-\theta)(\rho\boldsymbol{V})_c \cdot (\rho\boldsymbol{V})_{c^+} + (1-\theta)^2 (\rho\boldsymbol{V})_{c^+}^2 \right) \Bigg) \\
&= e_{\tilde{c}}^k + \frac{1}{2\rho_{\tilde{c}}} \Bigg(\frac{\theta \left(\rho_{\tilde{c}} - \theta\rho_c\right)}{\rho_c \rho_{\tilde{c}}} (\rho\boldsymbol{V})_c^2 \\
&\qquad - 2\theta(1-\theta) \frac{(\rho\boldsymbol{V})_c \cdot (\rho\boldsymbol{V})_{c^+}}{\rho_{\tilde{c}}} + (1-\theta) \frac{(\rho_{\tilde{c}} - (1-\theta)\rho_{c^+})}{\rho_{c^+}\rho_{\tilde{c}}} (\rho\boldsymbol{V})_{c^+}^2 \Bigg).
\end{aligned}$$

Finally by using the relation $\rho_{\tilde{c}} = \theta\rho_c + (1-\theta)\rho_{c^+}$ one obtains the following formulation of the corrected material internal energy

$$\left(e^k\right)_{\tilde{c}}^{corrected} = e_{\tilde{c}}^k + \frac{1}{2\rho_{\tilde{c}}} \left(\theta(1-\theta) \frac{\rho_c \rho_{c^+}}{\rho_{\tilde{c}}} \left(\boldsymbol{V}_c - \boldsymbol{V}_{c^+}\right)^2 \right), \qquad \theta \in [0,1]. \quad (12)$$

This last equation (12) demonstrates that the correction term keeps the positiveness of the remapped internal energy.

4.4 Time step control

The time step control follows [25] and is adapted to this ALE context. In practice, the time to compute the solution at time t^{n+1} starting from the solution at time t^n is chosen as

$$\Delta t^n = \min \left(C_v \Delta t_v^n, C_e \Delta t_e^n, C_n \Delta t^{n-1} \right),$$

where $C_e = 0.45$ (this value is the CFL default value and is specified depending on the test case), $C_v = 0.1$, $C_n = 1.1$ and Δt^{n-1} corresponds to the time step of the previous iteration (to compute the solution at time t^n starting from the solution at time t^{n-1}). The first condition enforces a maximum variation of $C_v = 10\%$ of the cell volume during the Lagrangian step by setting

$$\Delta t_v^n = \min_c \left(\frac{v_c^n}{|\int_{\partial\omega_c} \boldsymbol{V}^n \cdot \mathbf{n} ds|} \right),$$

where the denominator in this last equation is defined by (1). The second condition has been established in [25] to ensure the positivity of the internal energy in a purely Lagrangian monomaterial case working with a perfect gas. This condition is extended to this ALE framework by setting

$$\Delta t_e^n = \min_c \left(\frac{v_c^n}{(a_c^n + ||\boldsymbol{V}_c^n||) \sum_k s_k} \right),$$

for the Lagrangian plus remapping time steps and the same condition with $\boldsymbol{V}_c^n = \mathbf{0}$ for the pure Lagrangian ones. Finally, the last criterion simply ensures that the time step variation is not too steep during two time iterations (here a 10% time step variation).

Remark. In this 3D context an efficient parallelization procedure is mandatory. The parallelism aspects are addressed with standard MPI domain decomposition strategies. No particular design choices are made to address parallelization issues. In practice, material and average quantities are synchronized between processors corresponding to contiguous domains before each Lagrangian and remapping steps.

5 Numerical test cases

The various test cases presented in this section are concerned with stiffened gas and perfect gas equations of state. The stiffened gas equation of state (of which the perfect gas equation of state is a specific case) writes as follows

$$p = (\gamma - 1)\rho e - \gamma\pi,$$

The parameter π is homogeneous to a pressure and allows to take into account attraction between molecules. The coefficient γ, is known as the polytropic

index of the gas. The corresponding expression of the speed of sound reads

$$a^2 = \gamma \frac{p + \pi}{\rho}.$$

When $\pi = 0$, the stiffened gas equation of state reduces to the well-known perfect gas equation of state. We start this test section with two standard tests to assess the compressive limiter methodology.

5.1 Pure remapping test: Zalesak's disk case

This test is taken from [51] and consists in a simple advection test. The main objective of this section is to study the behavior of the compressive limiter. To achieve this, numerical results obtained with a standard second order remapping are compared with those obtained from the compressive limiter strategy. For this advection problem, a given velocity field is used to move the mesh nodes (the Lagrangian step is skipped) and the volume fraction profile is remapped onto the initial mesh.

A 2D space domain $[0, 1] \times [0, 1]$ is considered associated to a 2D velocity field of the form $\mathbf{V}(x, y) = (0.5 - y, x - 0.5)$. A disk shaped volume fraction with a small pocket is advected by this velocity field. More precisely, the initial volume fraction is defined by

$$\alpha(x, y) = \begin{cases} 1, & \text{if} \quad (||\mathbf{x} - \mathbf{c}|| < R) \quad \text{and} \quad (|x - c_x| \geq e \quad \text{or} \quad (y - c_y) > l), \\ 0 & \text{elsewhere,} \end{cases}$$

where $\mathbf{x} = (x, y)$, $\mathbf{c} = (0.5, 0.75)$ the space coordinates of the disk center and $R = 0.15$ its radius, $e = 0.025$ the width of the pocket and $l = 0.1$ its height. The initial profile is displayed in Figure 2. The initial volume fractions are set by computing the distances between the cell barycenters and the disk center. Depending if these distances are larger or smaller compared to the chosen radius, the corresponding cell volume fractions are set to 0 or 1. Several cartesian equidistant meshes are generated and the initial condition is set on them. A constant time step of 10^{-2} is used for all simulations.

The numerical results are presented in Figures 3 and 4 at time $t = 2\pi$ working with 128×128 and 256×256 cells. For both meshes, a direct comparison shows that the material interfaces at final time are much sharper (volume fraction profiles are less diffused) when using the compressive limiter strategy. These first results clearly demonstrate the interest in working

with compressive limiters for remapping volume fraction. It also noticed that for coarse meshes (here 128×128 cells), the volume fraction profiles obtained with the compressive limiters strategy remains diffused (the material interface is not completely sharp). Despite its compressive feature, the compressive methodology does not compete with a geometry based interface reconstruction strategy. As explained in introduction, for any mesh (coarse or refined), interface reconstruction based strategy are always more accurate than diffused interface methods. However, the compressive approach may be seen as an attractive compromise between accuracy (by considerably limiting the numerical smearing of the interfaces) and simplicity (compared to interface reconstruction strategies). It is also mentioned that the simulations are run by setting the initial material volume fractions to 0 or 1 with no need to add a small amount of one of the materials everywhere. In addition, in practise no overshoot (nor undershoot) is observed at the discontinuity since the modified Barth-Jespersen formula enforces the local minima and maxima by construction.

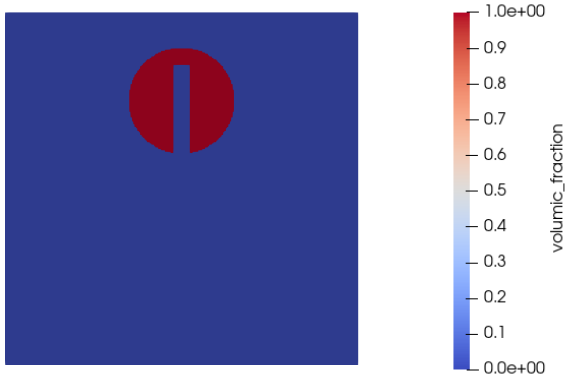

Figure 2: Representation of the initial volume fraction profile.

5.2 Pure remapping test: Kothe-Rider case

This text case is adapted from [58] and consists in a 3D advection test. The methodology follows the one presented in the last test as the main objective of this section is also to study the behavior of the compressive limiter. A $[0, 1]^3$ space domain is considered in which a sphere is set in a 3D velocity

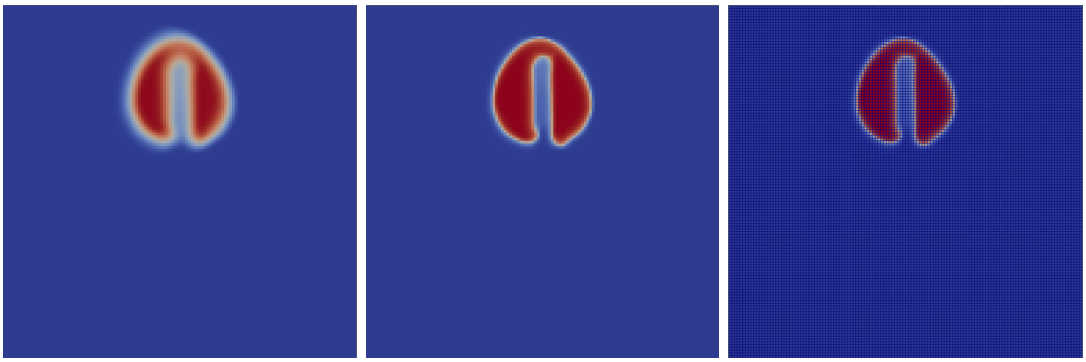

Figure 3: Numerical solution obtained for the second order remapping (left), compressive limiter strategy (middle) with a 128×128 mesh (displayed on the right picture).

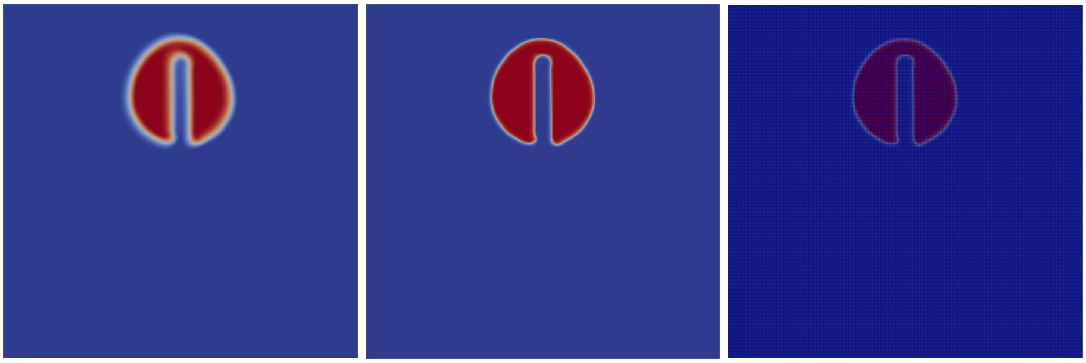

Figure 4: Numerical solution obtained for the second order remapping (left), compressive limiter strategy (middle) with a 256×256 mesh (displayed on the right picture).

field defined by

$$\mathbf{V}(t,x,y,z) = \begin{cases} 0, \\ \sin(\pi z)\cos(\pi z)\sin(\pi y)^2\cos(\pi t/t_f), \\ -\sin(\pi y)\cos(\pi y)\sin(\pi z)^2\cos(\pi t/t_f), \end{cases}$$

with the final time $t_f = 6$. The sphere radius is chosen to $R = 0.15$ and the center coordinates $(0.5, 0.5, 0.75)$. The initial profile in the plane $z = 0$ is displayed in Figure 5. The initial volume fractions are set by computing the distances between the cell barycenters and the sphere center. Depending

if these distances are larger or smaller compared to the chosen radius, the corresponding cell volume fractions are set to 0 or 1. A constant time step of 10^{-2} is used for all simulations. In Figure 6, for a $100 \times 100 \times 100$ mesh, the time evolution of iso-lines corresponding to the volume fraction $\alpha = 1$ is displayed. It is observed that for this test, the sphere (iso-lines corresponding to the volume fraction $\alpha = 1$) is first deformed by the velocity field then recombines to come back on its initial position.

The standard second order remapping is compared with the compressive limiter strategy. Several meshes have been used to study the numerical smearing. The results are displayed in Figures 7-9 for different meshes. For this test, despite the strong deformation, the initial sphere profile is supposed to be recovered at the end of the simulation. Because of the strong deformation, this test is relevant to study the numerical interfaces diffusion and in particular the behavior of the compressive limiters. The comparisons presented in Figures 7-9 clearly shows that the compressive limiters largely mitigate the numerical diffusion of the material interfaces. Despite the simplicity of the compressive strategy, the volume fraction profiles appear much sharper than the second order remapping ones. This 3D test, also confirms the observations made with the previous test. Indeed, it is noticed that for coarse meshes (here the $25 \times 25 \times 25$ and $50 \times 50 \times 50$ meshes), the numerical results obtained with the compressive limiters are still diffused. As explained for the previous test, despite the compressive feature, the compressive numerical strategy used does not compete with a geometry based interface reconstruction strategy.

5.3 Taylor-Green vortex

In this section the Taylor-Green vortex [23] test case is presented. It is a standard benchmark often used to assess the order of convergence of a numerical method. It consists in the simulation of a 2D stationary vortex flow on a domain $(x, y, z) \in [0, 1]^3$ initially filled with a perfect diatomic gas. Symmetry boundary conditions are applied to all boundaries. The flow is modelled by a divergence free velocity field $\mathbf{V}^0$ defined as follows

$$\mathbf{V}^0(x, y) = C_1 \begin{pmatrix} \sin(\pi x)\cos(\pi y) \\ -\cos(\pi x)\sin(\pi y) \end{pmatrix},$$

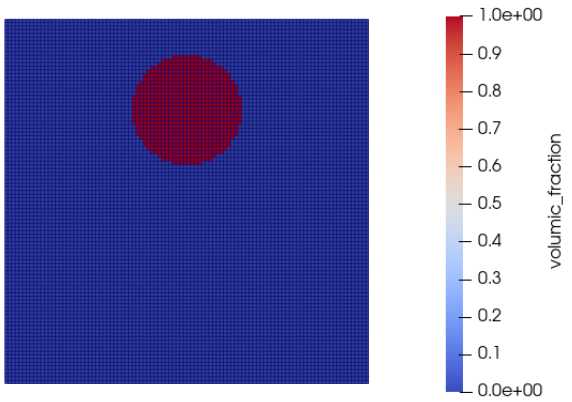

Figure 5: Representation of the initial volume fraction profile (plan taken at $z = 0$).

where C_1 is a constant. The associated pressure field writes

$$P^0(x, y) = \frac{1}{4}\rho^0 C_1^2 \big[\cos(2\pi x) + \cos(2\pi y) \big] + C_2,$$

where C_2 is an integration constant. In addition a source is added to the total energy evolution equation at eatch time step. It is defined as follows

$$S(x, y) = \frac{\pi}{4} \frac{\rho^0 C_1^3}{\gamma - 1} \big[\cos(3\pi x) \cos(\pi y) - \cos(3\pi y) \cos(\pi x) \big].$$

The constants are chosen such that $(\rho^0, C_1, C_2) = (1, 1, 1)$. The accuracy order of the Lagrangian scheme used in this document can be computed since the solution is regular and an exact solution is available. This test case is difficult for Lagrangian numerical methods since the mesh is distorted. In Figure 10, the pressure fields obtained with the Lagrangian scheme is displayed at at time $t = 0.5$ and $t = 0.7$. Following [25] the order of convergence is computed on the pressure field at time $t = 0.7$ using an unlimited second order procedure. This is only possible since the flow of the Taylor-Green Vortex is smooth and no oscillations arises from a possible discontinuity. The results are displayed in Figure 11. In Figure 11, the meshes used are denoted $n \times n$ even if in practise $n \times n \times 1$ meshes have been used. In addition, $\mathcal{E}_{L_p}$ and $\mathcal{O}_{L_p}$ denotes respectively the global error of convergence and the scheme

accuracy order in L_p norm. The errors are computed as follows

$$\mathcal{E}_{L_1} = \frac{1}{v_\omega}\sum_c v_c|\Delta P_c|, \quad \mathcal{E}_{L_2} = \sqrt{\frac{1}{v_\omega}\sum_c v_c|\Delta P_c|^2}, \quad \mathcal{E}_{L_\infty} = \max_c |\Delta P_c|,$$

where $v_\omega = \sum_c v_c$ corresponds to the total volume of the domain while v_c is the volume of cell ω_c. In addition, $\Delta P_c = P_c^{num} - P_c^{exact}$ is the difference in cell c between the pressure obtained by the numerical approximation and the exact value. The order of convergence $\mathcal{O}_{L_p}$ is computed with

$$\mathcal{O}_{L_p} = \frac{\log(\mathcal{E}^a_{L_p}) - \log(\mathcal{E}^b_{L_p})}{\log(\Delta x^a) - \log(\Delta x^b)},$$

where $\mathcal{E}^a_{L_p}$ and $\mathcal{E}^b_{L_p}$ are respectively the L_p errors computed on two meshes of characteristic length Δx^a and Δx^b.

5.4 Piston problem

To investigate the distribution of material entropy, a one-dimensional piston-driven compression problem is considered. At the left boundary of the computational domain, the fluid is compressed by a moving piston, which generates a right-propagating shock wave. The spatial domain is defined as $[0, 1]$, and the initial conditions are specified as

$$\begin{pmatrix} \alpha^1 \\ \rho^1 \\ \gamma^1 \\ p^1 \\ V \end{pmatrix}(t=0) = \begin{pmatrix} 0.9 \\ 1 \\ 1.4 \\ 1 \\ 0 \end{pmatrix}, \qquad \begin{pmatrix} \alpha^2 \\ \rho^2 \\ \gamma^2 \\ p^2 \\ V \end{pmatrix}(t=0) = \begin{pmatrix} 0.1 \\ 1 \\ 1.648 \\ 1 \\ 0 \end{pmatrix},$$

with a constant inflow velocity of $V = 2$ enforced at the left boundary. Figure 12 presents the profiles of the quantities $\alpha^k\rho^k$ (top left), $\alpha^k p^k$ (top right), $m^k\varepsilon^k$ (bottom left), and $m^k T^k d\eta^k$ (bottom right) at time $t = 0.2$ for a uniform mesh of 100 cells. As expected, entropy variations are localized in the vicinity of the shock front, located at $x = 0.6$ at this time. Furthermore, the majority of entropy dissipation is observed in material 1, consistent with the initially prescribed material volume fractions, which appear in the material dissipation matrices. The magnitude and distribution of entropy dissipation are in quantitative agreement with theoretical expectations. Finally, a wall-heating effect is observed near the left boundary, which is a well-known artifact of Lagrangian schemes.

5.5 Air-water shock tube

In this section a 1D simulation of a air-water shock tube in studied [52]. Because of the large compressibility difference between the fluids, this test is challenging. It is interesting since the robustness of the scheme is tested in addition to its ability to capture standard waves (rarefaction, shock, contact) despite the stiffness of the problem. For this test an exact solution is available.

The computational domain $\Omega = [0, 1]$ is filled with water (left side of the domain) and air (right side of the domain). Stiffened gas equation of state is used for the liquid while standard perfect gas closure is considered for the gas. More precisely, the following initial conditions are used

$$(\rho, V, p, \gamma, \pi) = \begin{cases} (10^3, 0, 10^9, 4.4, 6 \times 10^8) & \text{if} \quad x < 0.7, \\ (5, 0, 10^5, 1.4, 0) & \text{elsewhere.} \end{cases}$$

The final computation time is $t^f = 240 \times 10^{-6}$, a mesh of 1000 cells is used and the CFL number is set to 0.9. Density, velocity and pressure numerical results corresponding to time $t^f = 240 \times 10^{-6}$ are displayed in Figures 13, 14 and 15. The exact solution is displayed in blue. It is obtained by solving the exact Riemann problem and can also be found in [52]. The exact solution involves a rarefaction wave, a contact wave and a shock wave. The Lagrangian solution (no remapping) is displayed in red while the Eulerian one (remapping at each time iteration and compressive limiter activated $\beta = 2$) is in green.

It is observed that the Lagrangian and Eulerian strategies are both in good agreement with the exact solution. On the zoomed solution pictures (right column Figures) small overshoots and undershoots are observed for the velocity and pressure. It is also noticed that the numerical results presented in this document are similar to the ones obtained with explicit second order version of the scheme presented in [52] (also given with 1000 cells).

5.6 Triple point test cases

5.6.1 2D multi-material triple point

The multi-material triple point problem in 2D planar geometry [12] is now studied. This numerical test case is interesting in order to assess the robustness of an ALE method. The initial computational domain is rectangular and composed of three regions whose 2D dimensions are depicted in Figure

16 with the associated initial conditions. Symmetry boundary conditions are used for all boundaries. The initial grid consists in a $280 \times 1 \times 120$ cartesian mesh and the final time of the simulation is $t = 5$.

A CFL number of 0.4 is used. For this simulation, the Lagrangian code crashes after only few time iterations. Indeed, it is known that for this test, the strong mesh deformation makes the Lagrangian approach particularly unadapted. In Figure 17 and 18 the density and internal energy profiles are displayed at time $t = 5$ obtained with an Eulerian simulation (solution remapped to the initial mesh at each time iteration). It is observed that the overall structure is accurately captured with limited numerical dissipation at the material interfaces. In Figure 19 and 20 the numerical results obtained with the ALE strategy (here the regularisation procedure is run at each time step) are presented. The results are similar to the one obtained by remapping the solution on the initial mesh at each time step.

5.6.2 3D multi-material triple point

In this section a 3D version of the previous 2D triple point problem is presented. While this test case seems similar to the previous one, it is a real 3D configuration (the previous could be run with a 2D code). The only difference comes from the initial geometry of the third material which now occupy half of the domain in the depth direction which is now three. In Figures 21, 22 and 23 the density, internal energy profiles and volume fraction profile (of material 1) are displayed at time $t = 5$ for a $140 \times 60 \times 60$ mesh. Finally, the results of an ALE simulation are presented in Figure 24 where the density and internal energy profiles are displayed working with a 3D moving mesh made of $70 \times 30 \times 30$ cells. The main objective is to show that the numerical strategy can naturally be used for moving mesh simulations. The rezoning procedure is performed every 5-time iteration (after 5 Lagrangian steps) and only 1 rezoning step is used (1 iteration in the regularisation process). The moving ALE mesh obtained at final time is also displayed in Figure 25.

5.7 Air-Helium shock/bubble interaction test

5.7.1 Cylindrical bubble

The interaction of a shock travelling through the air with a spherical bubble of Helium is studied [44]. To this goal, a rectangular domain of dimensions

$[-0.13, 0.7] \times [0, 0.0445]$ initially full of Air characterized by $(\rho^1, p^1, \gamma^1) = (1.4, 10^5, 1.4)$ is considered. This domain also contains a spherical bubble of Helium $(\rho^2, p^2, \gamma^2) = (0.25463, 10^5, 1.648)$ modeled by a half disc centered in $(0, 0.0445)$ of radius 0.025 as depicted on Figure 26 (left picture). Wall boundary conditions are respectively chosen for the left and top boundaries. A piston-like condition is imposed to the right one for an incoming velocity equal to $\mathbf{V}^\star = (u^\star, 0)$. The horizontal velocity $u^\star$ is computed thanks to Rankine-Hugoniot conditions and is given by $u^\star = -105.4956563679$. The air after the shock is characterized by $(\rho^3, p^3, \gamma^3) = (1.92691, 1.5698 \cdot 10^5, 1.4)$. A CFL number of 0.4 is used. The mesh used consists of $1600 \times 320 \times 1$ cells. When the shock impacts the Helium gas, the cylinder is deformed.

The final density results are presented in Figure 26 (right picture). Schlieren profiles (density gradient profiles) are often displayed for this test. They are presented in Figures 27 and 28. These figures are obtained by directly using a post-processing tool to compute the density gradient profiles starting from the density results [52, 44]. It is observed that the material interfaces are accurately captured at all times. It is also remarked on the Schlieren profile figures that some waves are reflected on the input and output boundaries (right and left boundaries). This is due to the initial conditions which are enforced on these boundaries at all times. For this test, Kelvin-Helmholtz type instabilities develop at the interface between the two gases. It is observed that the scheme is able to reproduce the large scale and finer flow structures, while maintaining a sharp interface throughout the simulation.

5.7.2 Spherical bubble

In this section a 3D version of the previous 2D air-helium problem is presented. While this test case seems similar to the previous one, it is now a real 3D configuration (the previous could be run with a 2D code). The space domain is now $[-0.13, 0.7] \times [0, 0.0445] \times [0, 0.0445]$. The mesh used consists of $400 \times 80 \times 80$ cells. The final time is $t = 674 \cdot 10^{-6}$. The only difference with the previous test comes from the initial geometry since a spherical geometrical shape is used for the bubble. In Figures 29 and 30 the density and volume fraction profiles are displayed at initial times. In Figure 31 the volume fraction profiles are displayed at different times. For this test, the numerical results obtained with different mesh refinements are also given in Figure 32 using the compressive limiter ($\beta = 2$ on the left column) and no compressive limiter (right column). Even if the interfaces are diffused (espe-

cially for the coarser meshes), for each mesh, the impact of the compressive limiter is clearly observed with a sharper interface when using the limiter. This demonstrates the interest of strategy presented. Finally, the results of an ALE simulation are also given in Figure 33 where the volume fraction profile is displayed working with a 3D moving mesh made of $200 \times 40 \times 40$ cells. For this simulation, the rezoning procedure is performed every 5-time iteration (after 5 Lagrangian steps) with 5 rezoning steps (5 iterations in the regularisation process). The moving ALE mesh obtained at final time is displayed in Figure 34.

6 Conclusion

A cell-centered indirect Arbitrary Lagrangian-Eulerian diffuse interface strategy has been presented for solving a 3D multi-material model. It has been shown that the internal energy formulation, chosen for the multi-material Lagrangian step, enables to control each material entropy production. An anti-diffusive limiter has been used to prevent an excessive numerical diffusion during the material volume fractions remapping. This strategy has been detailed because of its simplicity (compared to standard 3D geometrical based interface reconstructions. The numerical test cases presented show that this approach constitutes an attractive compromise between accuracy (by limiting the numerical smearing of the material interfaces) and simplicity. To address the discrete total energy conservation issue, following [21, 2] the total kinetic energy is remapped to correct the material internal energies. It has then been proved that the material internal energies corrections are positive thus enforcing thermodynamics consistency. Finally, stiff multi-material test cases are investigated. Tests involving fluids with contrasted equations of state have been presented. This demonstrates the robustness of the overall numerical strategy. Various perspectives can be considered. In a near future, extensions to model multi-material configurations involving hypoelastic and hyperelastic materials will be investigated.

Acknowledgment. This work is supported by the U.S. Department of Energy (DOE), Office of Science, Fusion Energy Sciences, under Award No. DE-SC0024863: IFE-STAR and AWD-00007026: INFUSE.

References

[1] A. Colaïtis, S. Guisset and J. Breil. A Cell-Centered Amr-Ale Framework for 3d Multi-Material Hydrodynamics. Part I: Lagrangian and Indirect Euler Amr Algorithms. http://dx.doi.org/10.2139/ssrn.5167115. *Submitted for publication.*

[2] A. Marboeuf, A. Claisse and P. Le Tallec. Conservative and entropy controlled remap for multi-material ale simulations with space-staggered schemes. *J. Comput. Phys.*, 390:66–92, 2019.

[3] Ebenezer Mayowa Adebayo, Panagiotis Tsoutsanis, and Karl W. Jenkins. A review of diffuse interface-capturing methods for compressible multiphase flows. *Fluids*, 10, 2025.

[4] G. Allaire, S. Clerc, and S. Kokh. A five-equation model for the simulation of interfaces between compressible fluids. *J. Comput. Phys.*, 181(2):577–616, 2002.

[5] R. W. Anderson, V. A. Dobrev, T.V. Kolev, R.N. Rieben, and V.Z. Tomov. High-Order Multi-Material ALE Hydrodynamics. *SIAM J. Sci. Comput.*, 40(1):B32–B58, 2018.

[6] B. Després and F. Lagoutière. Contact discontinuity capturing schemes for linear advection and compressible gas dynamics. *J. Sci. Comp.*, 16:479–524, 2001.

[7] B. Manach-Pérennou, R. Chauvin, S. Guisset and A. Llor. Cell-centered Lagrangian scheme for multi-material flows with pressure equilibration. *Comput. and Fluids*, 250:105705, 2023.

[8] B. Manach-Pérennou, R. Chauvin, S. Guisset and J.P. Perlat. A simple strategy for multi-material diffusion and its application to three-temperature multi-material flows. *Commun. Comput. Phys.*, 38:1–36, 2025.

[9] M.R. Baer and J.W. Nunziato. A two-phase mixture theory for the deflagration-to-detonation transition (ddt) in reactive granular materials. *Int. J. Multiph. Flow*, 12(6):861–889, 1986.

[10] T.J. Barth and D.C. Jespersen. The design and application of upwind schemes on unstructured meshes. *AIAA Paper, 27th Aerospace Sciences Meeting, Reno, Nevada*, 89-0366, 1989.

[11] D.J. Benson. Computational methods in Lagrangian and Eulerian hydrocodes. *Comput. Methods Appl. Mech. Eng.*, 99:235–394, 1992.

[12] J. Breil. *Numerical methods for Lagrangian and Arbitrary-Lagrangian-Eulerian Hydrodynamic Contribution to the simulation of High-Energy-Density-Physics Problems*. Habilitation à diriger des recherches, Bordeaux University, https://hal.science/tel-01467157., 2016.

[13] D.E. Burton, N.R. Morgan, T.C. Carney, and M.A. Kenamond. Reduction of dissipation in Lagrange cell-centered hydrodynamics (CCH) through corner gradient reconstruction (CGR). *J. Comput. Phys.*, 299:229–280, 2015.

[14] E.J. Caramana, D.E. Burton, M.J. Shashkov, and P.P. Whalen. The construction of compatible hydrodynamics algorithms utilizing conservation of total energy. *J. Comput. Phys.*, 146:227–262, 1998.

[15] G. Carré, S. Del Pino, B. Després, and E. Labourasse. A cell-centered Lagrangian hydrodynamics scheme on general unstructured meshes in arbitrary dimension. *J. Comput. Phys.*, 228:5160–5183, 2009.

[16] R. Chauvin, S. Guisset, B. Manach-Pérennou, and L. Martaud. A colocalized scheme for three-temperature grey diffusion radiation hydrodynamics. *Commun. Comput. Phys.*, 31(1):293–330, 2022.

[17] A. Chiapolino, R. Saurel, and B. Nkonga. Sharpening diffuse interfaces with compressible fluids on unstructured meshes. *J. Comput. Phys.*, 340:389–417, 2017.

[18] V. Chiravalle, A. Barlow, and N.R. Morgan. 3D Cell-centered hydrodynamics with subscale closure model and multi-material remap. *Comput. and Fluids*, 207:104592, 2020.

[19] E. Heulhard de Montigny. *Thermo-hydro-dynamic consistency and stiffness in general compressible multiphase flows*. PhD thesis, Paris-Saclay University, https://theses.hal.science/tel-03821804., 2021.

[20] E. Heulhard de Montigny and A. Llor. Taming the "stiff stiffness" of pressure work and equilibration in numerical schemes for compressible multi-fluid flows. *Int. J. Multiph. Flow*, 153:104078, 2022.

[21] R. DeBar. Fundamentals of the KRAKEN code. *Technical Report UCIR-760*, 1974.

[22] B. Després and C. Mazeran. Lagrangian gas dynamics in dimension two and Lagrangian systems. *Arch. Ration. Mech. Anal.*, 178:327–372, 2005.

[23] V.A. Dobrev, T.V. Kolev, and R.N. Rieben. High-order curvilinear finite element methods for Lagrangian hydrodynamics. *SIAM J. Sci. Comput.*, 34:606–641, 2012.

[24] S. Galera, P.-H. Maire, and J. Breil. A two-dimensional unstructured cell-centered multi-material ALE scheme using VOF interface reconstruction. *J. Comput. Phys.*, 229:5755–5787, 2010.

[25] G. Georges, J. Breil, and P.-H. Maire. A 3D GCL compatible cell-centered Lagrangian scheme for solving gas dynamics equations. *J. Comput. Phys.*, 305:921–941, 2016.

[26] S.K. Godunov, A. Zabrodine, M. Ivanov, A. Kraiko, and G. Prokopov. Résolution numérique des problèmes multi-dimensionnels de la dynamique des gaz. *Éditions Mir Moscou*, 1979.

[27] S. Guisset, G. Damour, and J. Breil. Cell-centered indirect Arbitrary Lagrangian-Eulerian numerical strategy for solving 3D gas dynamics equations. *J. Comput. Phys.*, 505:112903, 2024.

[28] P. Hoch. An Arbitrary Lagrangian-Eulerian strategy to solve compressible fluid flows. *HAL: hal-00366858, version 1, 2009. Available at: http:// hal.archives-ouvertes.fr/docs/00/36/68/58/PDF/ale2d.pdf*, 2009.

[29] P. Hoch and E. Labourasse. A frame invariant and maximum principle enforcing second-order extension for cell-centered ALE schemes based on local convex hull preservation. *Int. J. Numer. Meth. Fluids*, 76:1043–1063, 2014.

[30] M. Ishii. Thermo-fluid dynamic theory of two-phase flow. *France: Eyrolles.*, 1975.

[31] A. Huerta J. Donea, J. Ph. Ponthot, and A. Rodriguez-Ferran. Encyclopedia of Computational Mechanics, volume 1: Fundamentals, Chapter 14: Arbitrary Lagrangian-Eulerian Methods,. *John Wiley and Sons*, 2004.

[32] J. Yao and D. Stillman. An equal-space algorithm for block-mesh improvement. *Procedia Engineering*, 163:199–211, 2016.

[33] S. S. Jain, M. C. Adler, J. R. West, A. Mani, P. Moin, and S. K. Lele. Assessment of diffuse-interface methods for compressible multiphase fluid flows and elastic-plastic deformation in solids. *J. Comput. Phys.*, 475:111866, 2023.

[34] P. Knupp. Achieving finite element mesh quality via optimization of the Jacobian matrix norm and associated quantities. Part I - A framework for surface mesh optimization. *Int. J. Numer. Methods Eng.*, 48 (3):401–420, 2000.

[35] P. Knupp and S. Steinberg. Fundamentals of Grid Generation. *CRC Press, Boca Raton*, 1993.

[36] A. Llor, A. Claisse, and C. Fochesato. Energy preservation and entropy in lagrangian space- and time-staggered hydrodynamic schemes. *J. Comput. Phys.*, 309:324–349, 2016.

[37] M. Worner. A compact introduction to the numerical modeling of multiphase flows. *FZKA*, 6932, 2003.

[38] P.-H. Maire, R. Abgrall, J. Breil, and J. Ovadia. A cell-centered Lagrangian scheme for two-dimensional compressible flows problems. *SIAM J. Sci. Comput.*, 29:1781–1824, 2007.

[39] V. Maltsev, M. Skote, and P. Tsoutsanis. High-order methods for diffuse-interface models in compressible multi-medium flows: A review. *Physics of Fluids*, 34(2):021301, 2022.

[40] L.G. Margolin. Introduction to an Arbitrary Lagrangian-Eulerian computing method for all flow speeds. *J. Comput. Phys.*, 135 (2):198–202, 1997.

[41] L.G. Margolin and M. Shashkov. Second-order sign-preserving remapping on general grids. *J. Comput. Phys.*, 184:266–298, 2003.

[42] S. Mirjalili, C. B. Ivey, and A. Mani. Comparison between the diffuse interface and volume of fluid methods for simulating two-phase flows. *Int. J. Multiph. Flow*, 116:221–238, 2019.

[43] A. Murrone and H. Guillard. A five equation reduced model for compressible two phase flow problems. *J. Comput. Phys.*, 202(2):664–698, 2005.

[44] S. Peluchon. *Approximation numérique et modélisation de l'ablation liquide.* PhD thesis, Bordeaux University, 2017.

[45] L. Qian, D.M Causon, C.G. Mingham, and D.M. Ingram. A free-surface capturing method for two fluid flows with moving bodies. *Proc. R. Soc. A.*, 462(2065):21–42, 2006.

[46] A. Robinson, T. Brunner, S. Carroll, R. Drake, C. Garasi, T. Gardiner, T. Haill, H. Hanshaw, D. Hensinger, D. Labreche, R. Lemke, E. Love, C. Luchini, S. Mosso, J. Niederhaus, C. Ober, S. Petney, W. Rider, G. Scovazzi, O. Strack, R. Summers, T. Trucano, V. Weirs, M. Wong, and T. Voth. ALEGRA: An Arbitrary Lagrangian-Eulerian Multimaterial, Multiphysics Code. 2012.

[47] S. Jaouen and F. Lagoutière. Numerical transport of an arbitrary number of components. *Comput. Methods Appl. Mech. Eng.*, 196(33-34):3127–3140, 2007.

[48] S. Kokh and F. Lagoutière. An anti-diffusive numerical scheme for the simulation of interfaces between compressible fluids by means of a five-equation model. *J. Comput. Phys.*, 229(8):2773–2809, 2010.

[49] R. Saurel and C. Pantano. Diffuse-interface capturing methods for compressible two-phase flows. *Annual Review of Fluid Mechanics*, 50:105–130, 2018.

[50] G. Scovazzi, J.N. Shadid, E. Love, and W.J. Rider. A conservative nodal variational multiscale method for Lagrangian shock hydrodynamics. *Comput. Methods Appl. Mech. Eng.*, 199:3059–3100, 2010.

[51] S.T. Zalesak. Fully multidimensional flux-corrected transport algorithms for fluids. *J. Comput. Phys.*, 31(3):335–362, 1979.

[52] L. Tallois, S. Peluchon, and P. Villedieu. A second-order extension of a robust implicit-explicit acoustic-transport splitting scheme for two-phase flows. *Comput. and Fluids*, 244:105531, 2022.

[53] J. Velechovsky, E. Kikinzon, N. Ray, H. Rakotoarivelo, A. Herring, M. Kenamond, K. Lipnikov, M. Shashkov, R. Garimella, and D. Shevitz. Multi-material swept face remapping on polyhedral meshes. *J. Comput. Phys.*, 469:111553, 2022.

[54] J. von Neumann and R.D. Richtmyer. A method for the numerical calculations of hydrodynamical shocks. *J. Appl. Phys.*, 21:232–238, 1950.

[55] M.L. Wilkins. Calculation of elastic plastic flow. *Methods Comput. Phys.*, 3:211–263, 1964.

[56] A. M. Winslow. Equipotential zoning of two-dimensional meshes. *Technical Report UCRL-7312*, 1963.

[57] A. M. Winslow. Numerical solution of the quasilinear poisson equation in a nonuniform triangle mesh. *J. Comput. Phys.*, 1(2):149–172, 1966.

[58] W.J. Rider and D.B. Kothe. Reconstructing volume tracking. *J. Comput. Phys.*, 141:112–152, 1998.

[59] J. Yao. A mesh relaxation study and other topics. *Lawrence Livermore National Laboratory Technical Report, LLNL-TR-637101*, 2013.

[60] D. Zuzio, J.-L. Estivalezes, P. Villedieu, and G. Blanchard. Numerical simulation of primary and secondary atomization. *Comptes Rendus Mécanique*, 341(1):15–25, 2013.

A Regularization step

In this Appendix, the regularization method presented in [27] and used here is recalled. This approach is inspired by the Line-Sweeping regularization method described in [59]. The Line-Sweeping regularization method consists in a local iterative geometrical process. More precisely, each node is moved

according to the position of its neighbors. As explained in [27], this regularisation method is limited to block-structured meshes. Now, since the work is devoted to 3D block-structured meshes, the indexes (i, j, k) are introduced to represent the three dimensions of space. A 2D stencil is a set of nodes obtained when one dimension index is i, j or k fixed. A 1D stencil is a set of nodes obtained if two dimensions indexes (i, j), (i, k) or (j, k) are fixed. This procedure is followed to extend the 1D method to multi-dimensional stencils.

For a given 1D stencil, the regularized position (new point coordinates) computed at iteration $m+1$ of a given node $\boldsymbol{x}_i^m$ (displayed in blue in Figure 35), the new node position is fixed $\boldsymbol{x}_i^{m+1}$ (displayed in red) at equal distance from the neighboring nodes $\boldsymbol{x}_{i-1}^m$ and $\boldsymbol{x}_{i+1}^m$ while following the geometry of the initial stencil. More precisely, after computing the length l^m of the branch (here the cell-index i is omitted in the length notations for more clarity)

$$l^m = l_1^m + l_2^m, \quad l_1^m = |\boldsymbol{x}_i^m - \boldsymbol{x}_{i-1}^m|, \quad l_2^m = |\boldsymbol{x}_i^m - \boldsymbol{x}_{i+1}^m|,$$

the regularized point position $\boldsymbol{x}_i^{m+1}$ (new point position) named "equal-space-point" is then defined as follows

$$\boldsymbol{x}_i^{m+1} = \left(\boldsymbol{x}_{i-1}^m + \frac{l^m}{2}\boldsymbol{e_1}\right)\delta_{\{\frac{l^m}{2} \leq l_1^m\}} + \left(\boldsymbol{x}_{i+1}^m + \frac{l^m}{2}\boldsymbol{e_2}\right)\delta_{\{\frac{l^m}{2} < l_2^m\}},$$

where we define

$$\boldsymbol{e}_1 = \frac{\boldsymbol{x}_i^m - \boldsymbol{x}_{i-1}^m}{|\boldsymbol{x}_i^m - \boldsymbol{x}_{i-1}^m|}, \qquad \boldsymbol{e}_2 = \frac{\boldsymbol{x}_i^m - \boldsymbol{x}_{i+1}^m}{|\boldsymbol{x}_i^m - \boldsymbol{x}_{i+1}^m|},$$

with the following notations

$$\delta_{\{\frac{l^m}{2} \leq l_1\}} = \begin{cases} 1 & \text{if} \quad \frac{l^m}{2} \leq l_1^m \\ 0 & \text{otherwise} \end{cases}, \qquad \delta_{\{\frac{l^m}{2} < l_2\}} = \begin{cases} 1 & \text{if} \quad \frac{l^m}{2} < l_2^m \\ 0 & \text{otherwise} \end{cases}.$$

It should be stressed that the new computed point has the advantage to be located on the initial geometry of the stencil. It is not the case if considering with a simple arithmetic average of the nodes $\boldsymbol{x}_{i-1}^m$ and $\boldsymbol{x}_{i+1}^m$. This simple but key idea enables to work with complex geometries (cylindrical geometry for example).

At this point, the regularization iteration index m are droped for clarity. In the case of a 2D stencil, each triplet of points forms a 1D stencil and may be used to compute a new point position fixed at equal distance from

the neighboring nodes. This new point is called the "equal-space-point" of the 1D stencil. In both directions of the 2D stencil six points can thus be computed. They are respectively denoted $\boldsymbol{x}_{j-1}$, $\boldsymbol{x}_j$, $\boldsymbol{x}_{j+1}$ in one direction and $\boldsymbol{x}_{k-1}$, $\boldsymbol{x}_k$ $\boldsymbol{x}_{k+1}$ in the other. These new points form two 1D stencils denoted $\{\boldsymbol{x}_{j-1}, \boldsymbol{x}_j, \boldsymbol{x}_{j+1}\}$ and $\{\boldsymbol{x}_{k-1}, \boldsymbol{x}_k, \boldsymbol{x}_{k+1}\}$. They are displayed in Figure 36. Again, two new points $\tilde{\boldsymbol{x}}_j$ and $\tilde{\boldsymbol{x}}_k$ are computed as the equal-space-point of the stencils $\{\boldsymbol{x}_{j-1}, \boldsymbol{x}_j, \boldsymbol{x}_{j+1}\}$ and $\{\boldsymbol{x}_{k-1}, \boldsymbol{x}_k, \boldsymbol{x}_{k+1}\}$. The final equal-space-point $\boldsymbol{x}$ in a 2D stencil is simply computed as the arithmetic average of $\tilde{\boldsymbol{x}}_j$ and $\tilde{\boldsymbol{x}}_k$ as displayed in Figure 37. This method naturally extends in 3D since each direction owns three 2D stencils. For each direction, three 2D-equal-space-points method are applied. We refer to [27, 32] for more details and mesh regularisation applications.

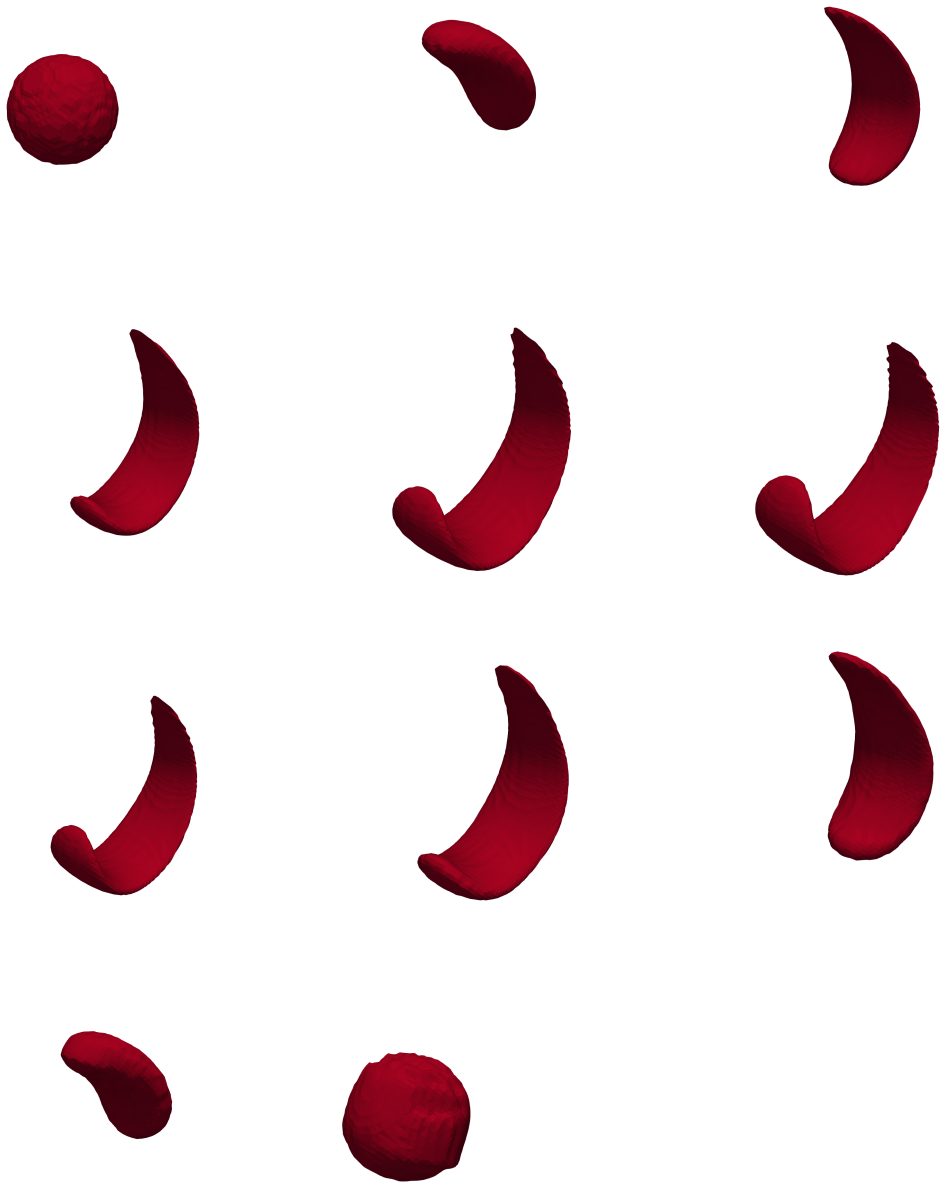

Figure 6: Illustration of the numerical volume fraction (iso-line corresponding to the volume fraction $\alpha = 1$) at various times (starting from left to right and top to bottom) for a $100 \times 100 \times 100$ mesh. The final profile (time $t_f = 6$) is displayed in bottom middle) and compared to the initial one (top left).

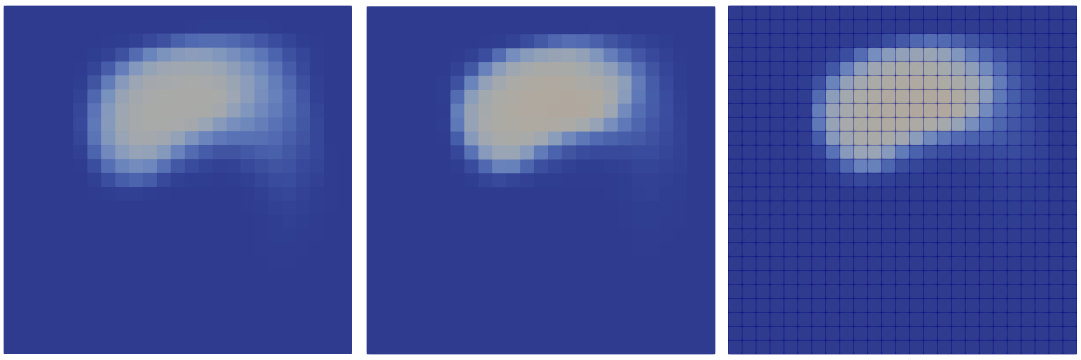

Figure 7: Numerical solution obtained for the second order remapping (left), compressive limiter strategy (middle) with a $25 \times 25 \times 25$ mesh (displayed on the right picture). Plan $z = 0$.

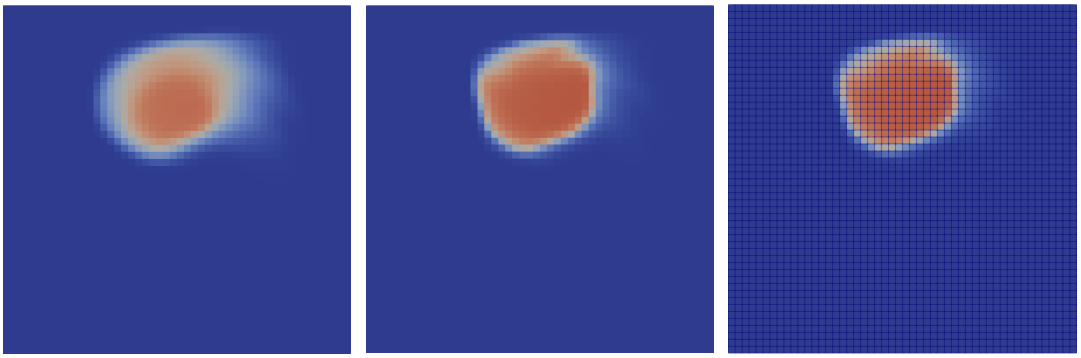

Figure 8: Numerical solution obtained for the second order remapping (left), compressive limiter strategy (middle) with a $50 \times 50 \times 50$ mesh (displayed on the right picture). Plan $z = 0$.

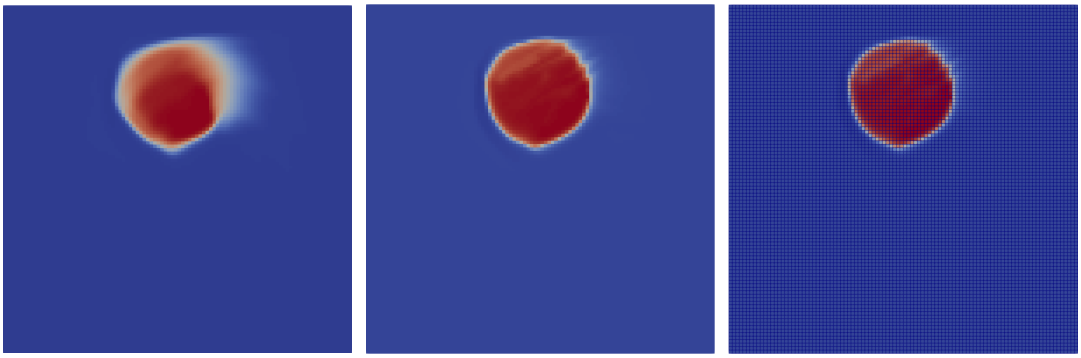

Figure 9: Numerical solution obtained for the second order remapping (left), compressive limiter strategy (middle) with a $100 \times 100 \times 100$ mesh (displayed on the right picture). Plan $z = 0$.

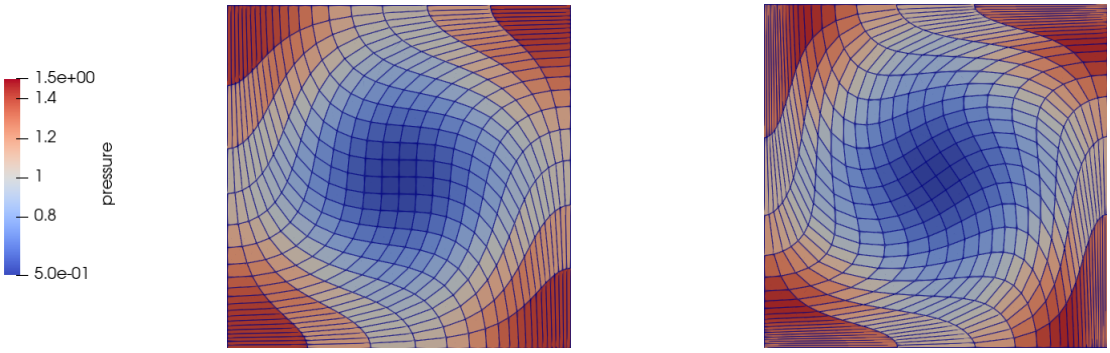

Figure 10: Pressure profiles obtained with the Lagrangian scheme working with a $20 \times 20 \times 1$ mesh at time $t = 0.5$ (left) and final time $t = 0.7$ (right).

Mesh	$\mathcal{E}_{L_1}$	$\mathcal{O}_{L_1}$	$\mathcal{E}_{L_2}$	$\mathcal{O}_{L_2}$	$\mathcal{E}_{L_\infty}$	$\mathcal{O}_{L_\infty}$
20×20	$2.97 \cdot 10^{-2}$	-	$3.79 \cdot 10^{-2}$	-	$1.02 \cdot 10^{-1}$	-
40×40	$1.54 \cdot 10^{-2}$	0.94	$1.82 \cdot 10^{-2}$	1.05	$3.86 \cdot 10^{-2}$	1.40
80×80	$4.49 \cdot 10^{-3}$	1.78	$5.43 \cdot 10^{-3}$	1.75	$1.16 \cdot 10^{-2}$	1.73
160×160	$1.10 \cdot 10^{-3}$	2.03	$1.38 \cdot 10^{-3}$	1.98	$4.27 \cdot 10^{-3}$	1.45
320×320	$2.80 \cdot 10^{-4}$	1.97	$3.44 \cdot 10^{-4}$	2.00	$1.33 \cdot 10^{-3}$	1.68

Figure 11: Table of convergence of the pressure field at final time $t = 0.7$ obtained with the Lagrangian scheme (no limitation).

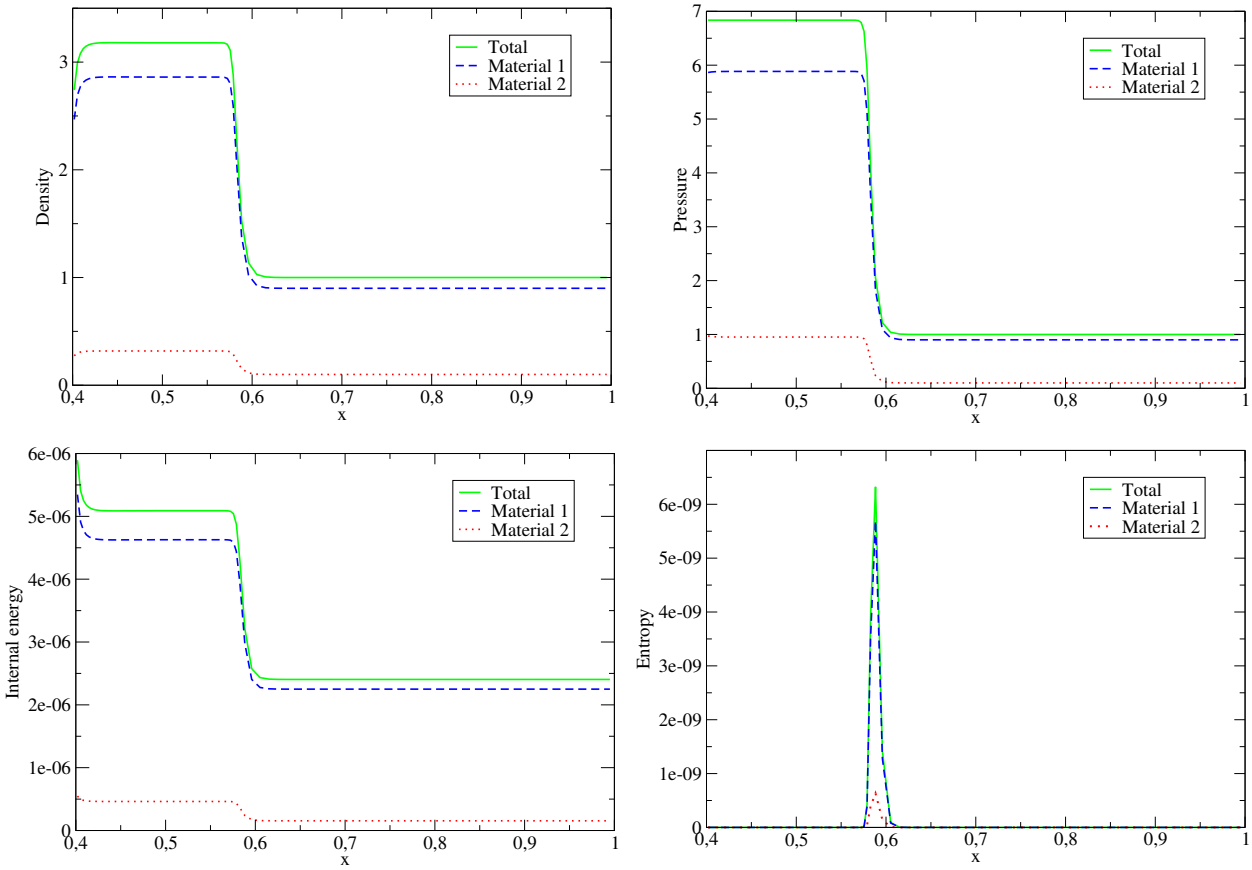

Figure 12: Piston test: profiles of the quantities $\alpha^k \rho^k$ (top left), $\alpha^k p^k$ (top right), $m^k \varepsilon^k$ (bottom left), and $m^k T^k d\eta^k$ (bottom right) at time $t = 0.2$, computed on a mesh of 100 cells.

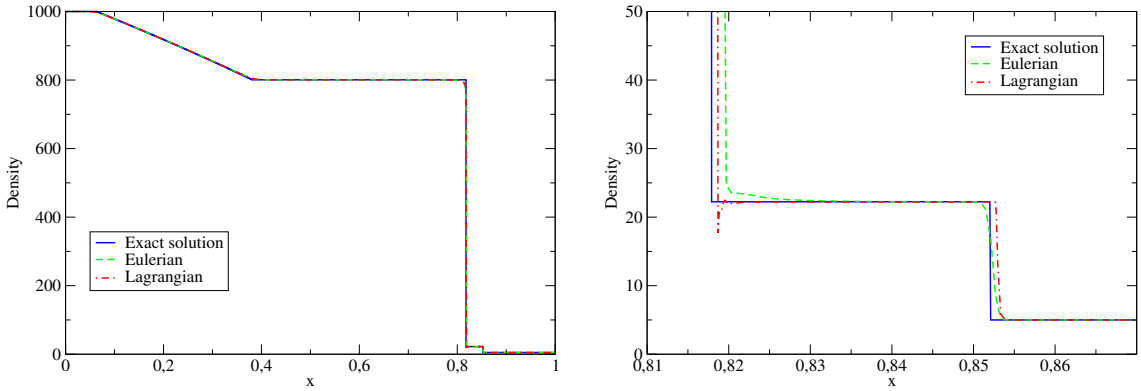

Figure 13: Density profiles obtained at time $t = 240 \cdot 10^{-6}$ with 1000 cells. Zoomed density profiles are displayed on the right picture.

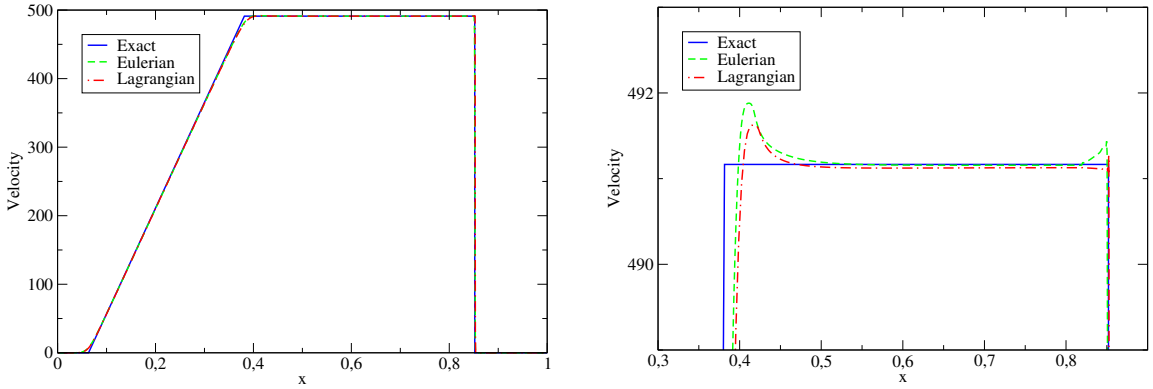

Figure 14: Velocity profiles obtained at time $t = 240 \cdot 10^{-6}$ with 1000 cells. Zoomed velocity profiles are displayed on the right picture.

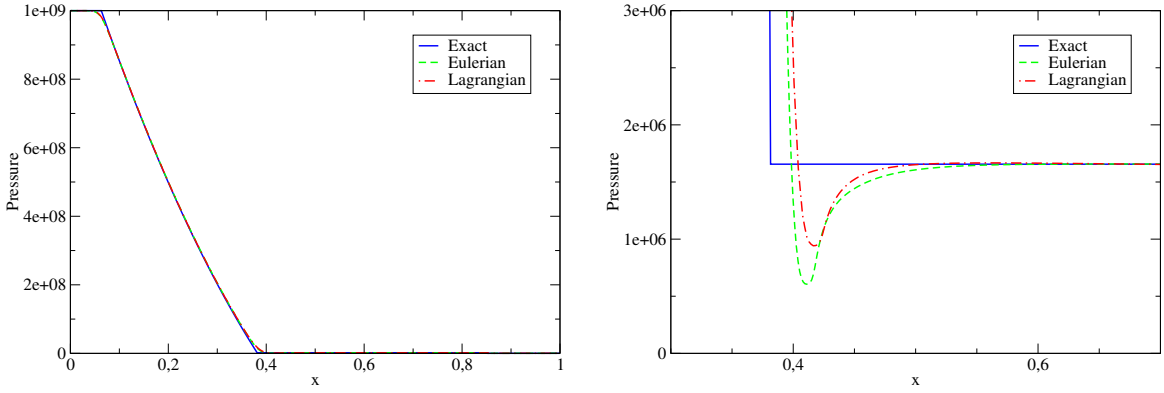

Figure 15: Pressure profiles obtained at time $t = 240 \cdot 10^{-6}$ with 1000 cells. Zoomed pressure profiles are displayed on the right picture.

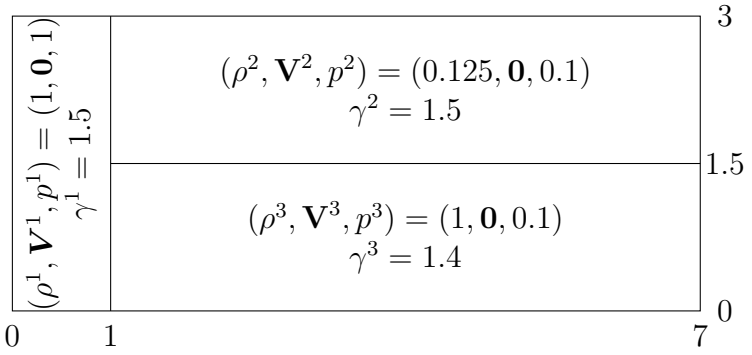

Figure 16: 2D triple point layout and associated initial conditions.

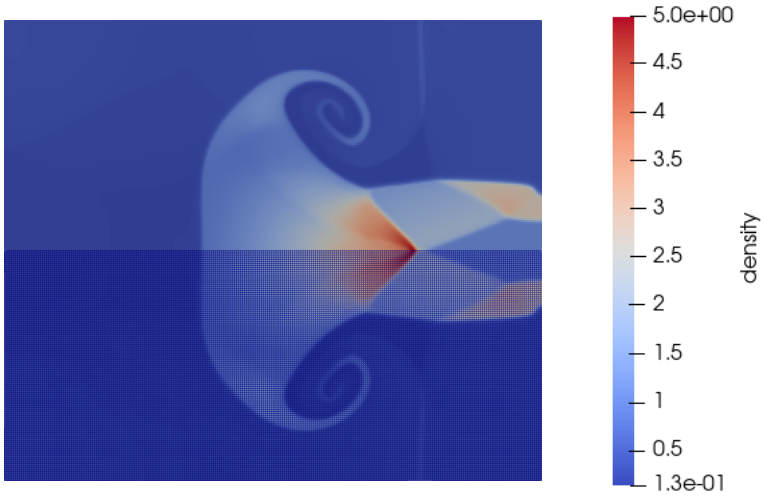

Figure 17: Density profiles obtained with an Eulerian simulation (the solution is remapped onto the initial mesh at each time iteration) in the case of a mesh made of $280 \times 120 \times 1$ cells at time $t = 5$. The mesh is displayed on the bottom Figure.

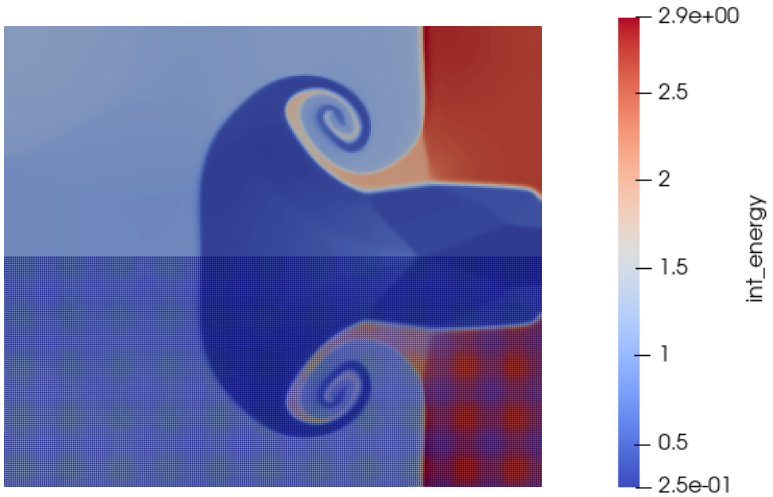

Figure 18: Internal energy profiles obtained with an Eulerian simulation (the solution is remapped onto the initial mesh at each time iteration) in the case of a mesh made of $280 \times 120 \times 1$ cells at time $t = 5$. The mesh is displayed on the bottom Figure.

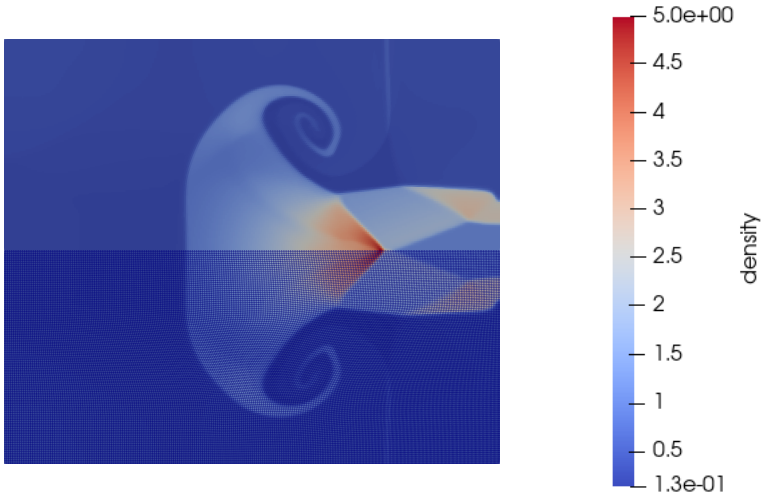

Figure 19: Density profiles obtained with $280 \times 120 \times 1$ cells at time $t = 5$ for an ALE simulation (for this simulation the regularisation procedure is applied at each time step). The mesh is displayed on the bottom Figure.

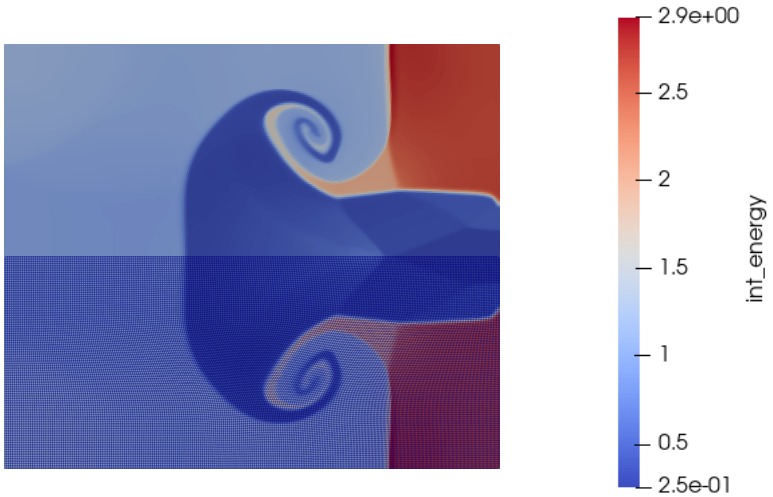

Figure 20: Internal energy profiles obtained with $280 \times 120 \times 1$ cells at time $t = 5$ for an ALE simulation (for this simulation the regularisation procedure is applied at each time step). The mesh is displayed on the bottom Figure.

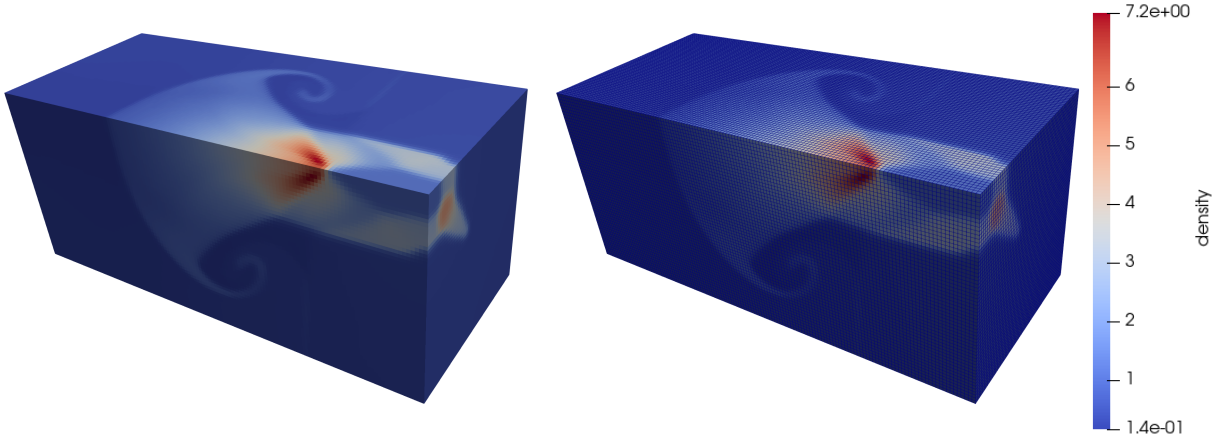

Figure 21: Density profile obtained with $140 \times 60 \times 60$ cells at time $t = 5$ for an (indirect) Euler simulation. The mesh is displayed on the right Figure.

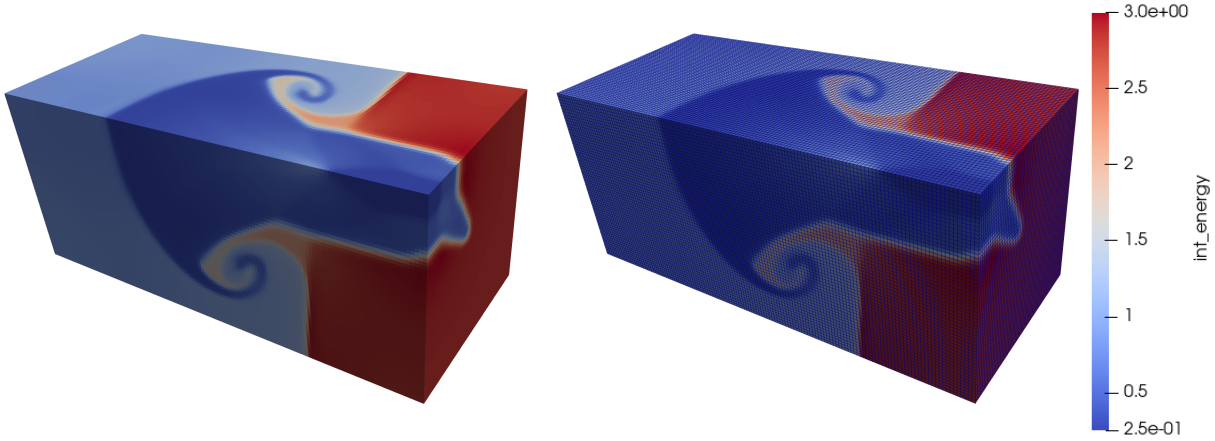

Figure 22: Internal energy profile obtained with $140 \times 60 \times 60$ cells at time $t = 5$ for an (indirect) Euler simulation. The mesh is displayed on the right Figure.

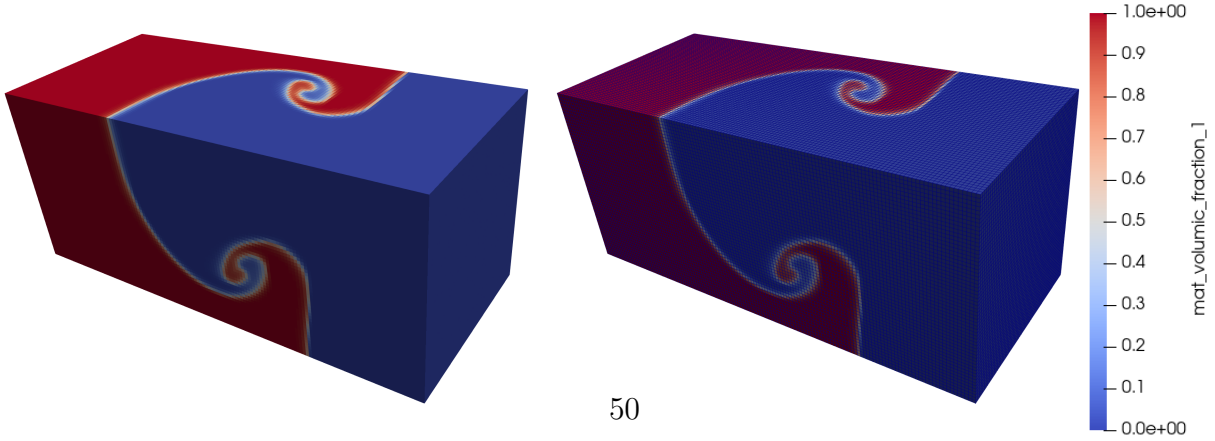

Figure 23: Volume fraction profile obtained with $140 \times 60 \times 60$ cells at time $t = 5$ for an (indirect) Euler simulation. The mesh is displayed on the right Figure.

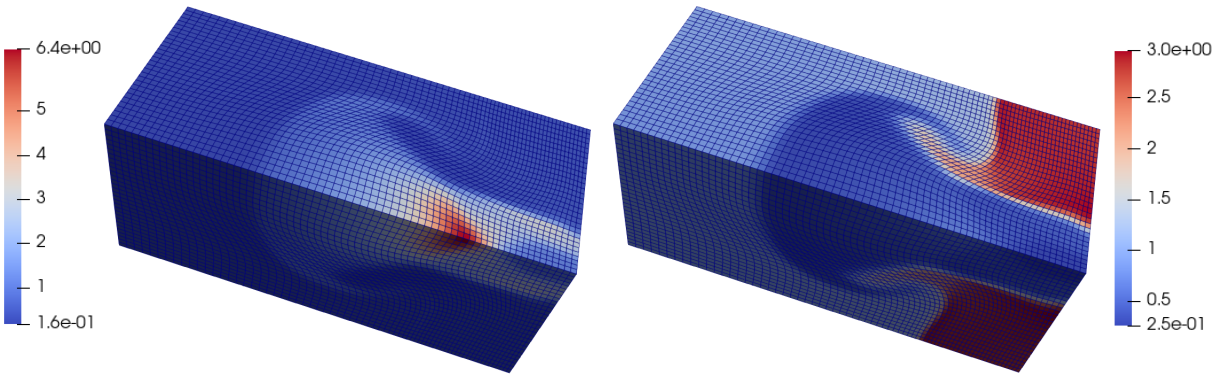

Figure 24: Density (left) and internal energy (right) profiles obtained with a $70 \times 30 \times 30$ moving mesh (ALE simulation).

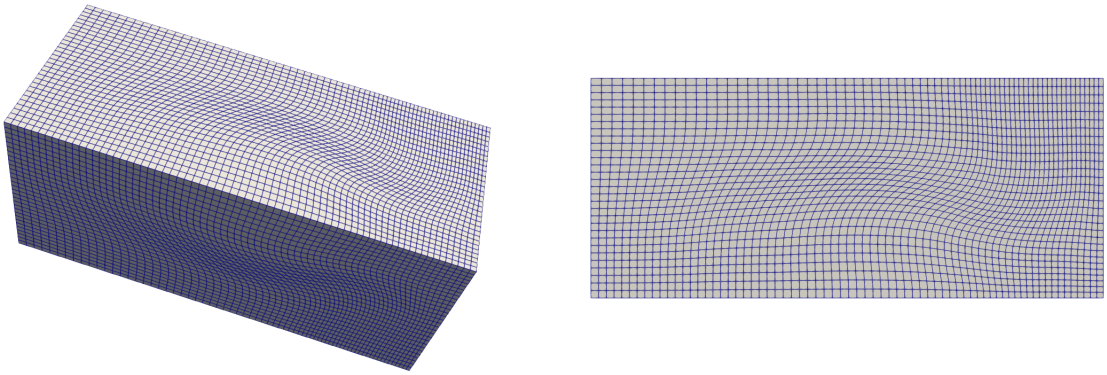

Figure 25: Representation of the final mesh obtained with a $70 \times 30 \times 30$ moving mesh (ALE simulation). A mesh view of the (x, z) plan at final time is displayed on the right Figure.

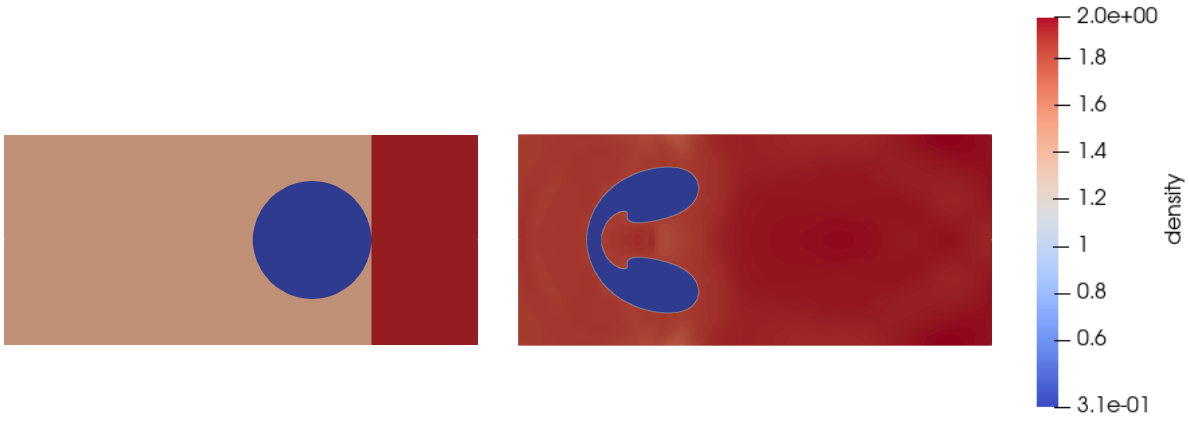

Figure 26: Density profiles at initial time and at final time $t = 674 \cdot 10^{-6}$. A mesh of 1600×320 cells is used for this (indirect) Euler simulation.

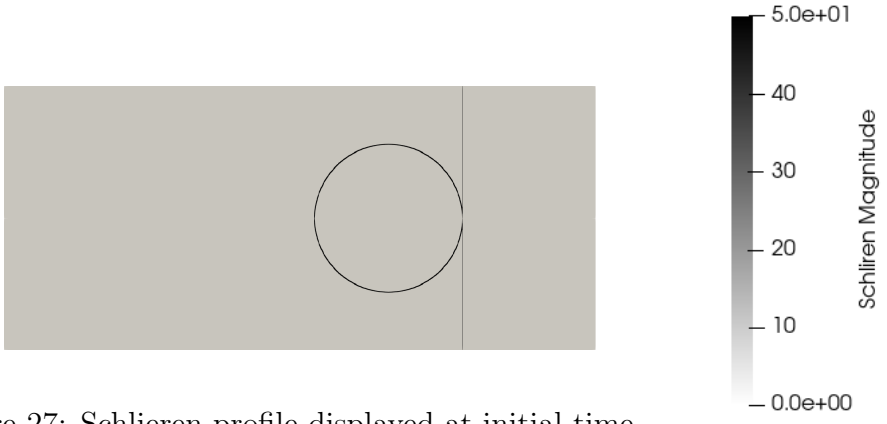

Figure 27: Schlieren profile displayed at initial time.

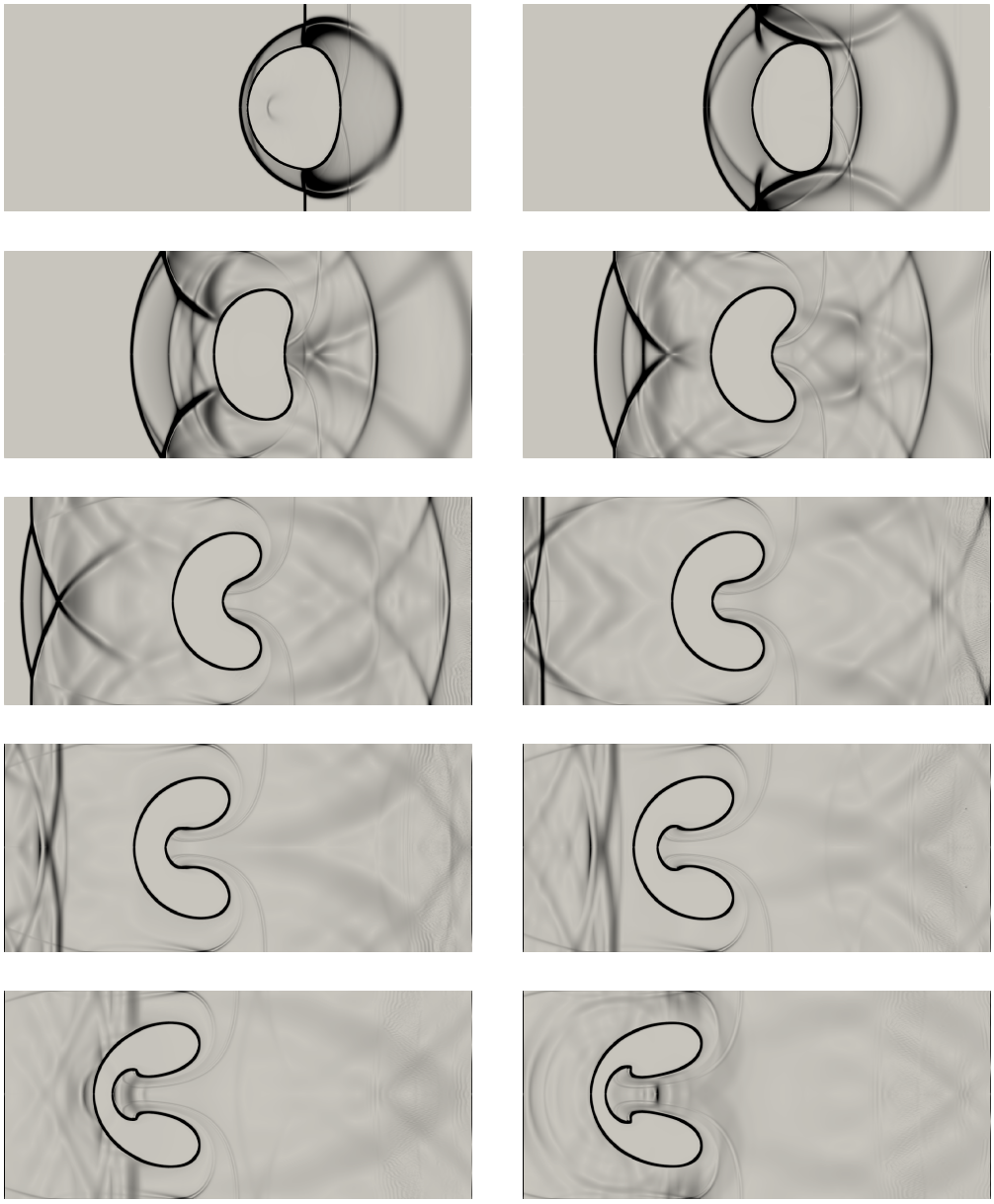

Figure 28: Schlieren profiles obtained at times $t = 67 \cdot 10^{-6}, 134 \cdot 10^{-6}, 202 \cdot 10^{-6}, 270 \cdot 10^{-6}, 337 \cdot 10^{-6}, 404 \cdot 10^{-6}, 472 \cdot 10^{-6}, 539 \cdot 10^{-6}, 607 \cdot 10^{-6}, 674 \cdot 10^{-6}$ (starting from left to right and top to bottom). A mesh of 1600×320 cells is used for this (indirect) Euler simulation.

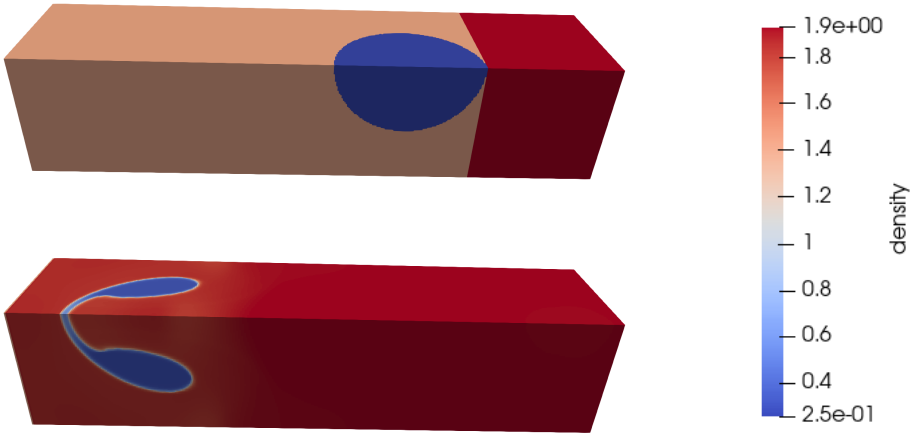

Figure 29: Density profile at initial time and at final time $t = 674 \cdot 10^{-6}$. A mesh of $400 \times 80 \times 80$ cells is used for this (indirect) Euler simulation.

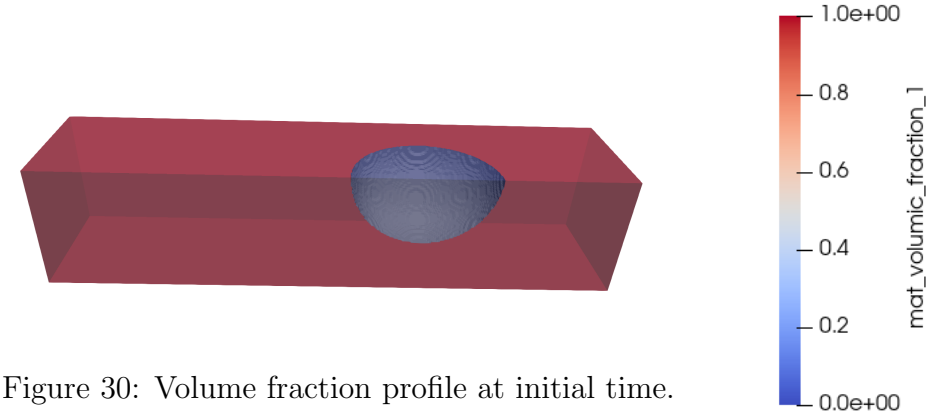

Figure 30: Volume fraction profile at initial time.

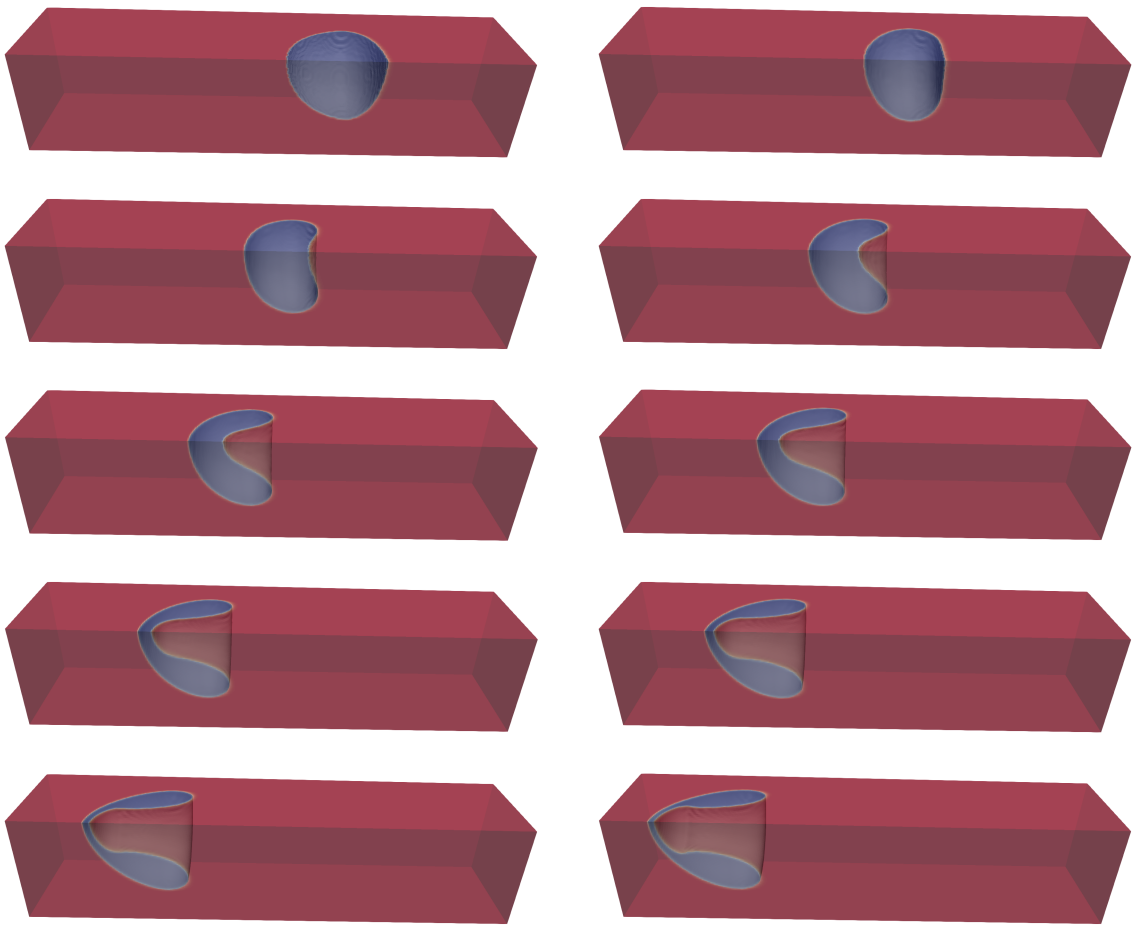

Figure 31: Volume fraction profiles obtained at times $t = 67 \cdot 10^{-6}, 134 \cdot 10^{-6}, 202 \cdot 10^{-6}, 270 \cdot 10^{-6}, 337 \cdot 10^{-6}, 404 \cdot 10^{-6}, 472 \cdot 10^{-6}, 539 \cdot 10^{-6}, 607 \cdot 10^{-6}, 674 \cdot 10^{-6}$ (starting from left to right and top to bottom). A mesh of $400 \times 80 \times 80$ cells is used for this (indirect) Euler simulation.

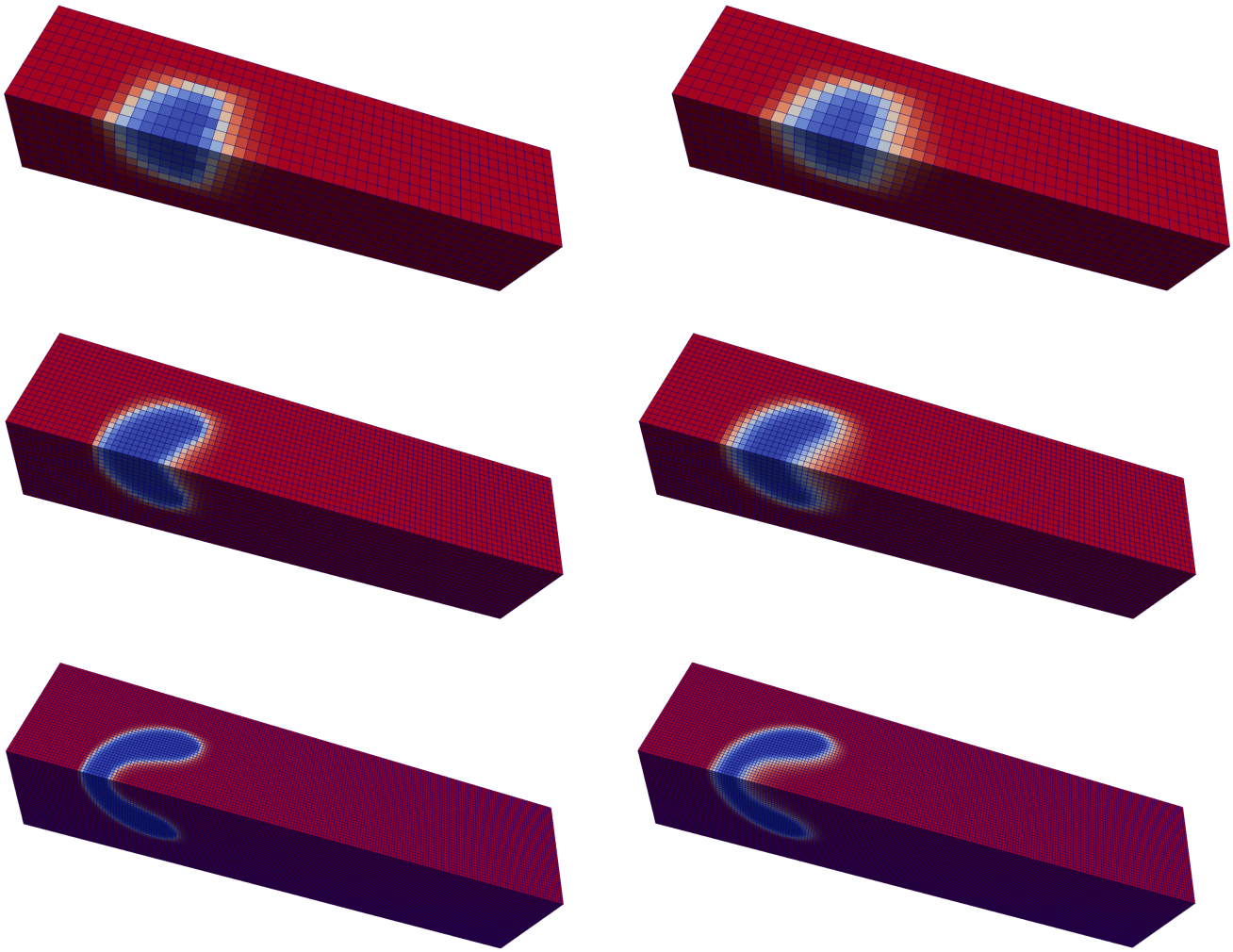

Figure 32: Volume fraction profiles obtained at final time $t = 640 \cdot 10^{-6}$ with Euler simulations using $50 \times 10 \times 10$ cells (top), $100 \times 20 \times 20$ cells (middle), $200 \times 40 \times 40$ cells (bottom) using the compressible limiter (left) and no compressive limiter (right).

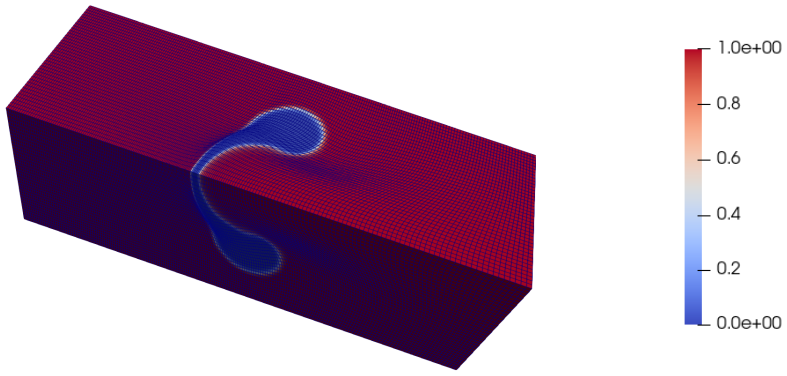

Figure 33: Volume fraction (right) profiles obtained at time $t = 640 \cdot 10^{-6}$ working with a $200 \times 40 \times 40$ moving mesh (ALE simulation).

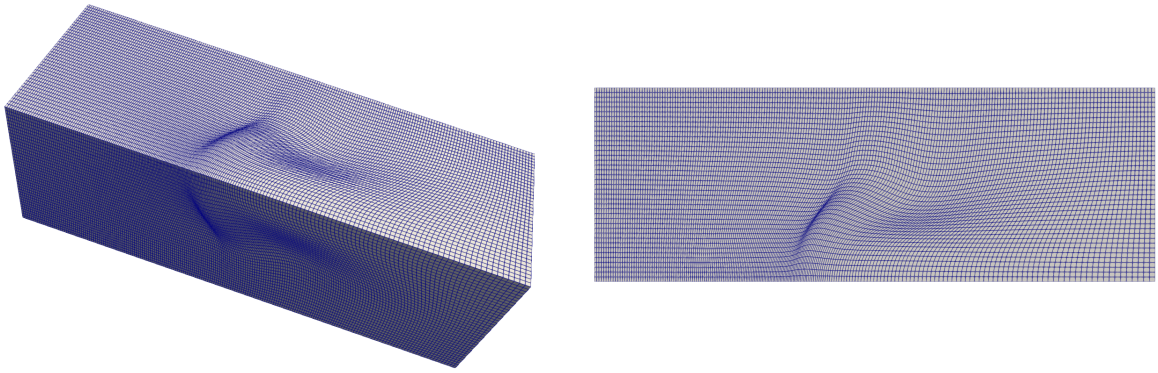

Figure 34: Representation of the final mesh obtained with a $200 \times 40 \times 40$ moving mesh (ALE simulation). A mesh view of the (x, z) plan at final time is displayed on the right Figure.

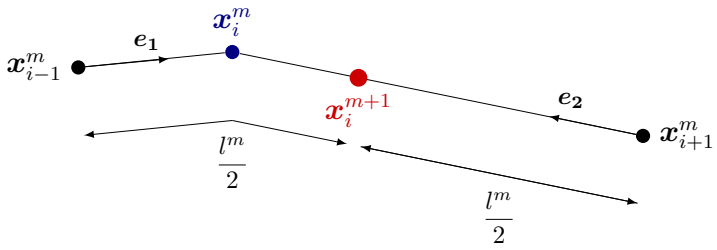

Figure 35: Regularization of a 1D stencil (1D equal-space-point method). The new node position $\boldsymbol{x}_i^{m+1}$ (red) is fixed at equal distance from the neighboring nodes $\boldsymbol{x}_{i-1}^m$ and $\boldsymbol{x}_{i+1}^m$ while following the geometry of the initial stencil.

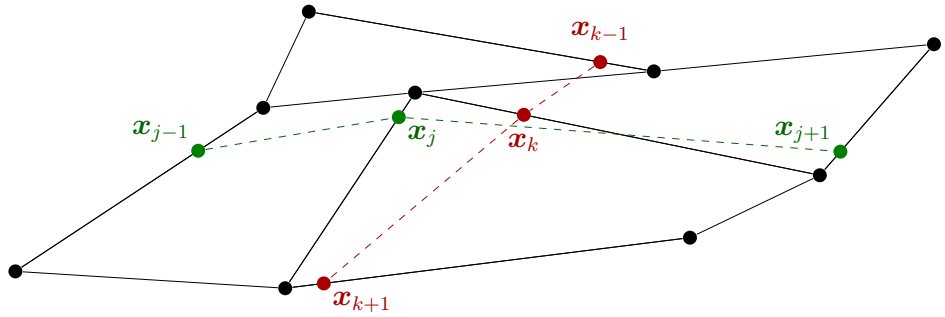

Figure 36: Regularization of a 2D stencil. Step 1: green and red points correspond to 1D equal-space-points in both directions. Two 1D stencils (one per direction) are then created.

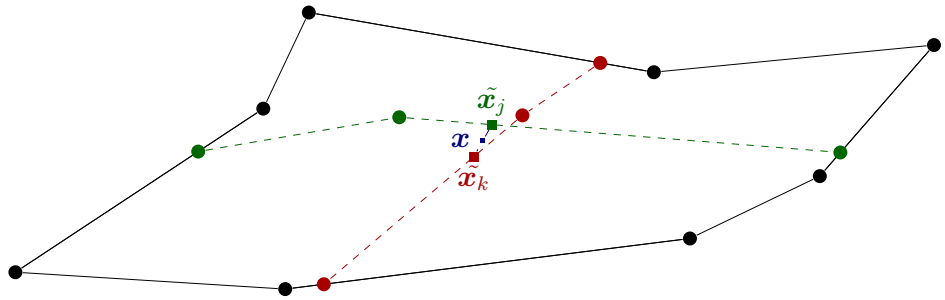

Figure 37: Regularization of a 2D stencil. Step 2: green and red points respectively denoted $\tilde{\boldsymbol{x}}_j$ and $\tilde{\boldsymbol{x}}_k$ correspond to each equal-space-point associated to each 1D stencil. The final regularization point $\boldsymbol{x}$ is computed with an arithmetic mean.